Bachelor of Science Thesis

# Pulsed Laser Deposition (PLD) and Characterisation of Gallium Oxide Heteroepitaxial Thin Films on Silicon Carbide

**Dilraaj Singh Hullon**

*Supervised by*

Jonas Johansson & Andri Dhora

Project duration: 3 months

Division of Solid State Physics

Department of Physics

Lund University

May 2026

**Abstract**

$\beta$-$Ga_2O_3$ ($\beta$-gallium oxide) is an ultra-wide band gap semiconductor material that has attracted significant interest for next-generation high-efficiency and high-power electronic devices. This thesis focuses on the optimisation of the growth of gallium oxide thin films on 1.0 cm x 1.0 cm silicon carbide (4H-SiC) using pulsed laser deposition (PLD).

A growth matrix in substrate temperature and oxygen chamber pressure was first investigated in order to understand the growth behaviour of gallium oxide on SiC and to identify the optimal conditions for the growth of films with both high crystalline quality and high growth rate. The growth temperature studied ranged from 700°C to 900°C, while the oxygen pressure was varied between 0.01 mbar and $1.14\times10^{-4}$ mbar. The introduction of an argon-grown buffer layer was found to be crucial for achieving high crystalline quality growth of gallium oxide on SiC. Consequently, thin buffer layers deposited for 1700 pulses at 700°C in 0.01 mbar argon pressure were incorporated into the subsequent optimisation series involving laser fluence and pulse frequency. The laser fluence was varied between 1.38 J/cm$^2$ and 1.98 J/cm$^2$, while the pulse frequency ranged from 2 Hz to 5 Hz. Increasing the thickness of the argon-grown buffer layer was furthermore found to improve the crystalline quality of films.

All films were characterised using X-ray diffraction (XRD), scanning electron microscopy (SEM), spectroscopic ellipsometry (SE), and atomic force microscopy (AFM). The optimised film was 108.07±0.33 nm thick, exhibited a growth rate of 10.8 pm/pulse, possessed a relatively smooth surface morphology ($R_q$ = 2.5 nm), and demonstrated a narrow ($\bar{2}01$) rocking curve full width at half-maximum (FWHM) of 1.627°± 0.034°.

## Acknowledgments

I am deeply thankful to my supervisor, Jonas Johansson, for allowing me to conduct my thesis under his guidance and supervision.

Thank you also to my co-supervisor, Andri Dohra, for all your support and help. I appreciate the time and effort that you put into assisting me with this thesis work.

Gratitude must also be extended to my family, friends and close one for their continued help and support during my thesis period.

I would like to acknowledge NanoLund and Myfab, as this work was made possible by their experimental resources.

# Contents

# 1 List of abbreviations

PLD - Pulsed Laser Deposition
MOVPE - Metal-Organic Vapour-Phase Epitaxy
MBE - Molecular Beam Epitaxy
HVPE - Hydride Vapour-Phase Epitaxy
XRD - X-Ray Diffraction
SEM - Scanning Electron Microscope
EDS - Energy-Dispersive X-ray Spectroscopy
AFM - Atomic Force Microscopy
RHEED - Reflective High-Energy Electron Diffraction
SE - Spectroscopic Ellipsometry
UV - Ultraviolet
UWBG - Ultra Wide Band Gap
DC - Direct Current
AC - Alternating Current
$Ga_2O_3$ - Gallium Oxide
Si - Silicon
SiC - Silicon Carbide
GaN - Gallium Nitride
Ga - Gallium
O - Oxygen
$\alpha$ - alpha
$\beta$ - beta
$\delta$ - delta
$\kappa$ - kappa
$\epsilon$ - epsilon
$\gamma$ - gamma
$\Phi$ - phi
$\omega$ - omega
$\Psi$ - psi
$\theta$ - theta
KrF - Krypton-Flouride
FVDM - Frank-Van der Merve
VW - Volmer-Weber
TS - Target-Substrate
CCD - Charged Coupled Detector
FWHM - Full Width at Half Maximum
BSE - Backscattered Electron
SE - Secondary Electron
MSE - Mean Square Error
IPA - Isopropanol
DI - Deionised
HF - Hydrofluoric acid

## 2 Introduction

Gallium oxide ($Ga_2O_3$) is an ultra-wide band gap semiconductor material that is more promising for high-power devices compared to traditional materials, such as silicon (Si) [1]. Its ultra-wide band gap translates to a higher breakdown electric field, leading to more efficient electrical energy conversion [2], reduced resource use, and more compact high-power electronics, such as power switches or converters [2]. Efficient power converters reduce electrical energy losses in the various conversion steps during transmission from generation to consumers [3], as shown in Figure 1 (a), enabling a more efficient use of the available electrical energy. This is a necessary step towards the electrification of society and to reduce carbon emissions (Figure 1 (b)) [2].

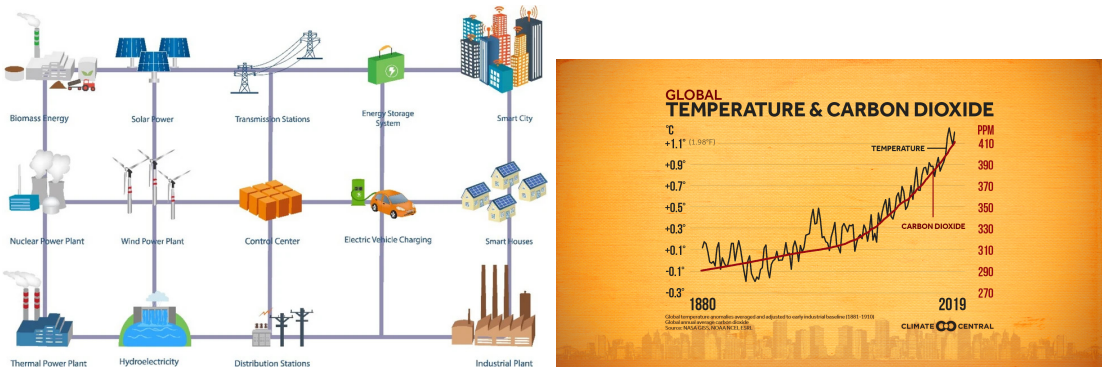


(a) (b)

Figure 1: (a) Electrification in a carbon-free society [4]. (b) Correlation between global temperature and carbon emissions (Credit: Climate Central).

In addition, gallium oxide is promising for other applications, such as solar blind photodetectors [5]. Solar blind photodetectors are devices that detect the presence of light that is not in the visible spectrum, mainly in the ultraviolet (UV) or infrared spectrum [6]. These detectors are important in areas where there is a need to detect UV light, without the measurement being influenced by visible light [6]. Some of the main applications of solar blind photodetectors include monitoring electricity discharge from power lines due to their UV emission or from a military application, the detection of hot gases from a missile's rocket motor when it is observed in a bright environment. The latter also uses the infrared emission of the hot gases to detect its heat signature [6].

To fulfill this potential, high crystal quality $Ga_2O_3$ crystals, developed at a high growth rate, are needed. There are various growth methods, each with its own advantages and disadvantages. These include metal-organic vapour-phase epitaxy (MOVPE), molecular beam epitaxy (MBE), and hydride vapour-phase epitaxy (HVPE) [5]. In this work, the method used is pulsed laser deposition (PLD). In PLD, laser light is used to eject material from a sintered target, leading to the formation of a plasma plume which shares the stoichiometry of the target [5], and to the subsequent formation (growth) of a thin film on a substrate [5]. This method of growth produces high-quality and high-purity $Ga_2O_3$ crystals at a relatively high growth rate [5]. These two factors are crucial in semiconductor growth. Another consideration is the cost, which is why the $Ga_2O_3$ crystals are grown on silicon carbide (SiC) substrates in this thesis work [7].

The objective of this thesis is to understand the growth behaviour of $\beta$-$Ga_2O_3$ and then optimize heteroepitaxial PLD growth of $\beta$-$Ga_2O_3$ thin films on SiC substrates, by determining the growth conditions for single-crystalline $\beta$-$Ga_2O_3$ films with high crystalline quality, smooth surface morphology, and high growth rates. These growth objectives are often difficult to achieve

simultaneously, as they tend to counteract one-another. In general, in crystal growth, increasing the growth rate can lead to reduced crystallinity, whereas highly crystalline films with smooth surfaces typically require slower growth conditions and therefore longer deposition times. As a result, the PLD growth parameters must be optimised to achieve a suitable balance between crystallinity, growth rate, and surface morphology.

To evaluate the resulting thin films, a number of complementary characterisation techniques are employed throughout this work. X-ray Diffraction (XRD) is used to assess the crystalline quality and the preferred orientation of the films on the substrate. Scanning Electron Microscopy (SEM) and Atomic Force Microscopy (AFM) are used to investigate the surface morphology across large and small surface areas, respectively. Reflective High-Energy Electron Diffraction (RHEED) and Spectroscopic Ellipsometry (SE) are used to determine the completion of the nucleation layer and film thickness, respectively. Together, these techniques provide a comprehensive understanding of the structural, morphological, and optical characteristics of the grown films.

# 3 Background

## 3.1 Gallium Oxide

Gallium oxide has six types of crystal structures, called polymorphs. These are the $\alpha$, $\beta$, $\delta$ $\epsilon$, $\kappa$, and $\gamma$ polymorphs [1]. Polymorphs are crystals with the same chemical composition, but different crystalline structures, orientations, and physical properties [8]. The $\beta$, $\alpha$, $\epsilon$, $\delta$ and $\gamma$ polymorphs assume the monoclinic, corundum (hexagonal), orthorhombic, cubic, and defective spinel crystal structures, respectively [1]. $\kappa$ gallium oxide also has an orthorhombic structure, similar to the $\epsilon$ polymorph [9].

Among all six polymorphs, the thermodynamically stable one is $\beta$-$Ga_2O_3$ [1]. The other polymorphs can be stabilised at lower temperatures but will convert to $\beta$-$Ga_2O_3$ at high enough temperatures [1]. This thesis will focus primarily on the growth of $\beta$-$Ga_2O_3$ as it is the most promising phase for high-power electronics. $\beta$-$Ga_2O_3$ has a monoclinic unit cell (Figure 2), with lattice constants, $a = 12.23\mathring{A}$, $b = 3.04\mathring{A}$, $c = 5.8\mathring{A}$ [10] [11].

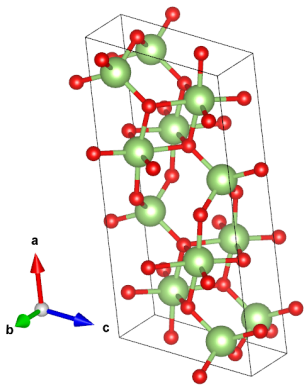


Figure 2: Unit cell of monoclinic $\beta$-$Ga_2O_3$ labelled with its a, b and c axes.

The main benefit of $\beta$-$Ga_2O_3$ is its ultra-wide band gap (4.9 eV [12]), which implies a large energy difference between the bottom of the conduction band and top of the valence band [1]. The generation of wide-band gap semiconductors, such as gallium nitride (GaN) and silicon carbide (SiC), have band gaps of 3.4 eV and 3.26 eV, respectively [12]. The wider band gap of $Ga_2O_3$ makes it more promising for high-power electronics [12].

The ultra-wide band gap enables a high breakdown electric field of approximately 8 MV/cm [12]. A high breakdown field is essential in power converters or switches, as it allows the blocking of high voltages in the OFF state, coupled with a low resistance in the ON state [13].

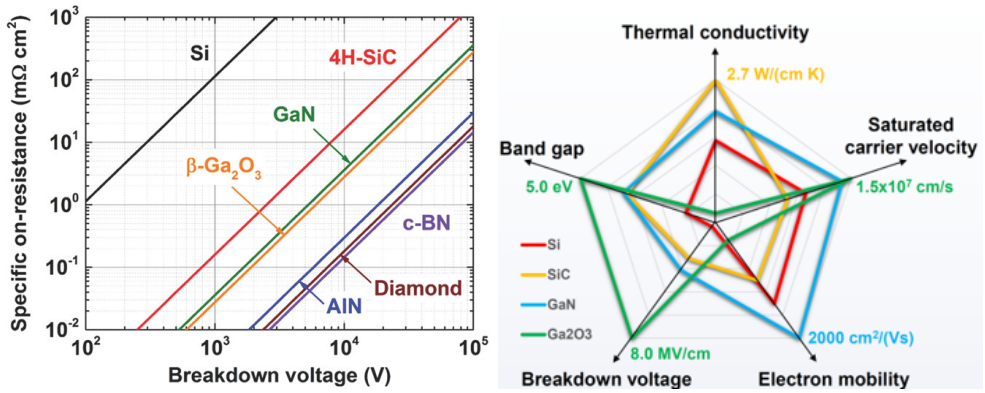


(a) (b)

Figure 3: (a) ON state resistance against breakdown voltage for different semiconductor materials [14]. (b) Physical properties of $Ga_2O_3$ compared to other semiconductor materials [13].

A lower ON state resistance allows for reduced conduction loss, which in turn allows for higher conversion efficiency in power converters [15]. As depicted in Figure 3(a), there is a tradeoff between breakdown voltage and ON state resistance, which is improved by the use of wider band-gap materials [13]. For this reason, $Ga_2O_3$ is a very promising semiconductor for high-power conversions (DC-AC, AC-DC) in various systems (photovoltaic, electric cars, data centers, etc) [16].

$Ga_2O_3$ suffers from the impossibility of p-type doping and from its low thermal conductivity, as shown in Figure 3(b) [14]. The lack of p-type doping is a result of deep acceptor energy levels when $Ga_2O_3$ is doped with common acceptor dopants (zinc, magnesium) [12]. This results in the prohibition of an increase in the concentration of holes, which results in the unsuccessful p-type doping of $Ga_2O_3$ [12]. Its low thermal conductivity may be tackled by the heteroepitaxy of $\beta$-$Ga_2O_3$ films on substrates of higher thermal conductivity (such as SiC), or by remote epitaxy on graphene grown on SiC [17]. Deposition of a stressor layer on top of the $\beta$-$Ga_2O_3$ film would allow for the mechanical exfoliation of the thin film from graphene [17]. This produces free-standing $\beta$-$Ga_2O_3$ films that can be subsequently bonded to substrates of higher thermal conductivity [17].

### 3.2 Pulsed Laser Deposition

$Ga_2O_3$ growth in this work is performed with Pulsed Laser Deposition (PLD). PLD is a physical vapour deposition process that uses the congruent ablation of a sintered target material via laser light, to allow for the formation of a stoichiometric plasma plume. This enables the subsequent growth of thin films on a given substrate that is situated above the target. Congruent ablation refers to the direct (non-thermal) evaporation of material from the target surface via the transfer of energy from the laser light to the material before equilibrium heating occurs, leading to the

formation of a stoichiometric plasma plume [18].

Photoexcitation occurs on the target's surface, producing electron-hole pairs that form (excited) metastable non-binding states on the surface [18]. They do not radiatively relax due to non-radiative defect reactions. Further photoexcitation results in non-thermal ejection of ions from the surface of the target [18]. This results in the formation of a stoichiometric plasma plume, which rises and expands adiabatically perpendicular to the target surface [19]. The plasma plume then rises higher and reaches the substrate, and the ions adsorb and react on the substrate surface. This results in the growth of thin films onto the surface of the substrate.

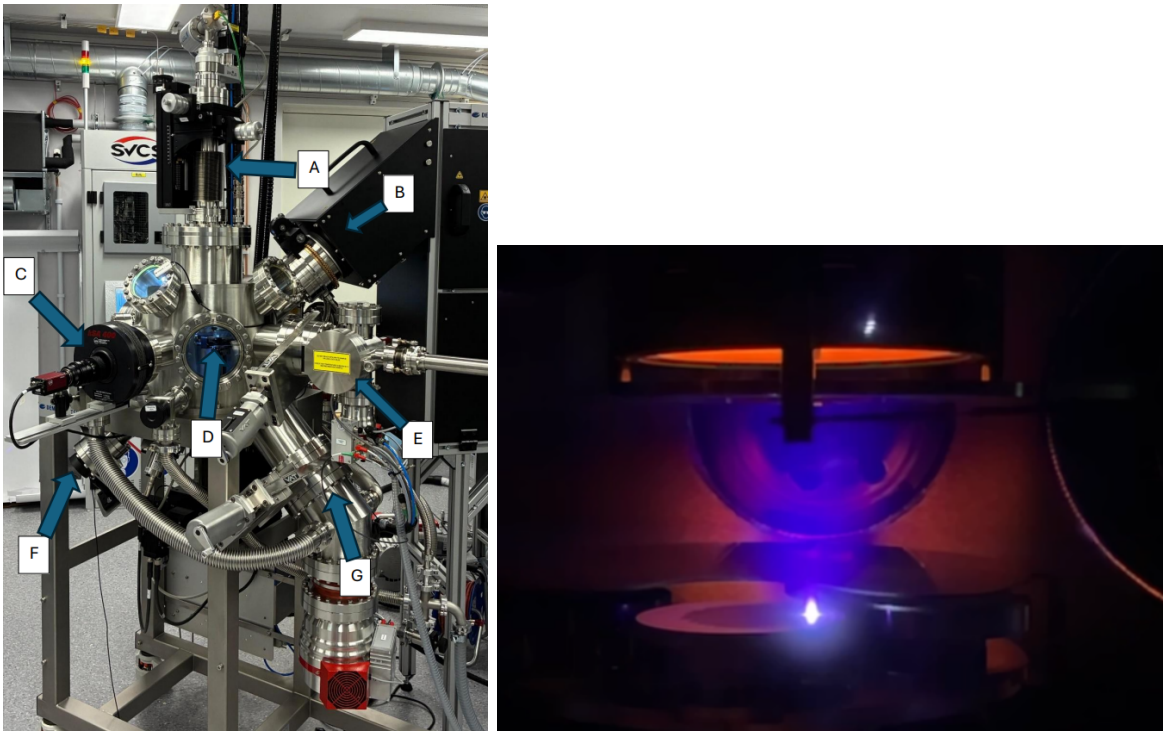


(a) (b)

Figure 4: (a) Pulsed Laser Deposition setup used for this thesis work. (b) Plasma plume in deposition chamber during growth run.

Figure 4 (a) shows a basic setup for a PLD apparatus. In modern PLD systems, excimer gas lasers (e.g., krypton-fluoride, KrF) are the most common [18]. The laser light is pulsed onto the target at a certain frequency that can be adjusted for the particular experiment. The spot size on the target and the energy of the laser light are important parameters, as there is a minimum threshold of energy density that needs to reach the target for congruent ablation of a given target material. The target should match the stoichiometry of the intended thin film. At the right growth conditions, the target stoichiometry can be exactly transferred to the thin film. The ability to grow highly pure thin films with the intended stoichiometry is a key advantage of PLD [20]. It is easy to switch between targets during growth, as most PLD setups allow for easy transfer of targets via a target holder carousel. Figure 4 (b) shows the plasma plume that is formed during a growth run.

From Figure 4 (a), the components of the PLD setup used include, A: Heater, and substrate holder height controller (used to change the height of the substrate for loading and unloading, and position the substrate for deposition), B: Excimer laser (used to ablate the gallium oxide target), C: RHEED electron detector (used to display electron diffraction pattern), D: Deposi-

tion chamber (used for deposition of thin films on substrate), E: Lock load chamber (used to load and unload target/substrate), F: Laser fluence detector (used to measure the laser fluence for ablation), G: Main turbo pump (used to generate vacuum in deposition chamber).

The actual growth occurs on the substrate, which is positioned above the target in our setup. The substrate chosen in our experiments is silicon carbide (SiC) due to its lower cost compared to native $\beta$-$Ga_2O_3$ substrates, high thermal conductivity, and ease of growing graphene via sublimation of Si - allowing for remote epitaxy of $\beta$-$Ga_2O_3$ on graphene-covered SiC. Heaters must also be used to increase the temperature of the substrate to allow for the growth of crystalline gallium oxide [18]. PLD growth can occur in vacuum or in the presence of a process gas. The vacuum is achieved via a combination of backing and turbo pumps.

There are some disadvantages to this thin-film fabrication technique, such as "splashing". The occurrence of splashing degrades the quality of thin-films, due to the incorporation of large particulates or droplets, resulting also in poor crystallinity and high surface roughness [19]. One source for splashing is target subsurface boiling. During ablation, the target subsurface layer may reach its boiling point and melt before the surface [19], resulting in the ejection of molten particle droplets that form on the surface. Another source of splashing is recoil pressure-induced removal, which occurs when the plasma shockwave induces a recoil force onto the target surface. As a result, the molten surface may spew out liquid particles that may incorporate on the substrate [19]. Reducing the laser energy, frequency, and using a denser target serve to reduce the chances of splashing occurring [19]. Furthermore, the scalability of PLD is worse compared to other deposition techniques, as the plasma plume extends only over a relatively small cross-sectional area. This limits growth uniformity over large area substrates [21]. However, a way to overcome this is to rotate and scan (raster) the substrate such that the plasma plume covers a wider area and allows for uniform growth on a large substrate [22]

As mentioned earlier, however, in addition to offering easy stoichiometric transfer of target material to the substrate, PLD enables growth of highly pure gallium oxide films, as only Ga and O ions are present in the chamber. The film purity is limited only to the purity of the target and precursor gases [18]. The PLD machine is also relatively easy to operate. These advantages are beneficial to students who are new to the deposition of thin films, which is the case in this thesis work.

### 3.3 Thin Film Growth

The objective of this thesis is the optimisation of the heteroepitaxial growth of $\beta$-$Ga_2O_3$ on c-plane SiC (001). There are two types of epitaxial growth, homoepitaxy and heteroepitaxy. Homoepitaxy is a form of epitaxial growth whereby the grown thin film matches the lattice constants and thermal expansion coefficients of the substrate [23]. In this specific case, the thin film and the substrate would both need to be $\beta$-$Ga_2O_3$. Heteroepitaxy, on the other hand, refers to the growth of thin films on a different material than the substrate on which they are grown [23].

When heteroepitaxy is conducted, one consideration to take into account is lattice mismatch [24]. Lattice mismatch refers to the difference in lattice constants between the thin film and the substrate [24]. Lattice constants refer to the size of a unit cell of a crystal, with a unit cell having at most 3 lattice constants to describe its 3-dimensional size [25]. A unit cell, on the other hand, is the most basic building block of the crystal, which is repeated and translated in every direction throughout a perfect crystal [25]. This means that the unit cells in $\beta$-$Ga_2O_3$ and (001) oriented SiC do not align perfectly. The result of this mismatch is a buildup of strain in the thin film. Strain energy increases as the thickness of the film increases, up to a critical thickness, above which the film plastically relaxes, leading to the formation of extended defects in the crystal lat-

tice - such as dislocations - which are detrimental to the electrical properties of the thin film [24].

The equation to determine the lattice mismatch (or, equivalently, the biaxial strain) between any two materials is given as a percentage in Equation 3.1:

$$\varepsilon_m\% = \left(1 - \frac{a_f}{a_s}\right) \times 100 \tag{3.1}$$

where, $a_f$ is the in-plane lattice constant for the thin film, and $a_s$ is the in-plane lattice constant for the substrate [18]. The lattice mismatch between $\beta$-$Ga_2O_3$ and SiC is 0.3% in the b direction and 6.9% in the a direction [26].

The oxygen atoms in $(\bar{2}01)$ planes of $\beta - Ga_2O_3$ share the same hexagonal (honeycomb) arrangement of Si on Si-face (001) oriented SiC. Therefore, to minimise lattice mismatch, $\beta$-$Ga_2O_3$ grows $(\bar{2}01)$ oriented on (001) oriented SiC.

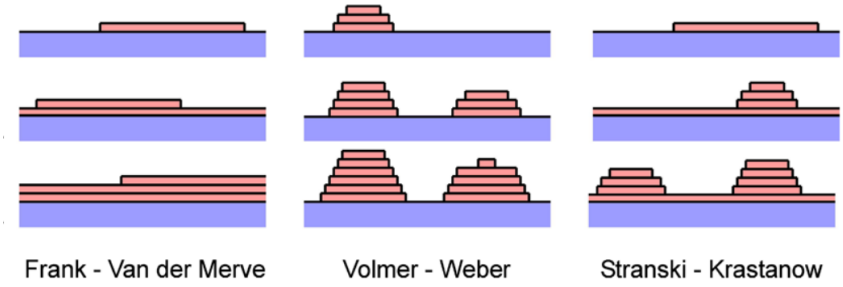


Figure 5: Growth modes in heteroepitaxial thin film growth [27].

There are 3 main growth modes, as shown in Figure 5: Frank-Van der Merve growth (2D), Volmer-Weber growth (3D), and Stranski-Krastanow growth (2D/3D) [27]. The Frank-Van der Merve (FVDM) growth mode occurs when the deposited atoms arrange themselves layer by layer in a 2-dimensional manner [19]. This happens when the cohesive force between the target atoms is weaker than the adhesive force between those atoms and the surface [19]. This results in the atoms favouring being deposited on the substrate in a layered manner. The resultant thin film is typically smooth (2D-like). FVDM growth necessitates high temperatures for a larger surface diffusion length of adatoms (atoms that adsorb, and diffuse on the film's surface), at the expense of growth rate [18].

The next growth mode is named after Volmer-Weber (VW). In this growth mode, the attractive force between the deposited atoms is stronger than their attraction to the substrate surface [19]. This results in the deposited atoms forming 3-dimensional islands, as it is more energetically favourable to do so rather than deposit uniformly over the entire surface [27]. This growth mode occurs at relatively low growth temperatures and results in rough films [18].

The third main growth mode is the Stranski-Krastanov growth mode, whereby the atoms deposit in a layer-by-layer mode first, and then, beyond a critical thickness, the growth proceeds in a 3D manner. This occurs when the force between deposited atoms is similar to the atom and surface force [19]. The deposition starts out as a layer (2D) deposition, and then beyond a critical thickness, the strain built up due to lattice mismatch relaxes elastically, resulting in the formation of strained 3D islands [18]. This results in rough thin films. The type of growth mode favoured in a particular experiment depends on the substrate used - whether the growth is homo-

or heteroepitaxial, the orientation of the grown film, temperature, pressure, laser fluence, and laser frequency [19]. In this thesis, the growth mode is predominantly FVDM at high growth temperatures; however it resembles 3D growth due to the formation of ($\bar{2}$01)-oriented domains.

### 3.4 Growth Parameters

In thin-film growth, the film growth rate and crystallinity are two key considerations. The former is crucial to determining throughput, and the latter is important to ensuring the crystal quality of the grown film for the best possible electrical properties. The parameters that influence growth rate and crystallinity include the oxygen pressure in the PLD chamber, the substrate temperature, laser fluence, and the distance between the target and substrate.

The first parameter to consider is chamber pressure. The typical pressure for the chamber ranges from 1 mbar to $10^{-9}$ mbar [18]. The overall pressure in the chamber has an effect on plasma dynamics and the resulting stoichiometry of the thin film. Ablation in our specific case involves two particles, gallium and oxygen ions, which both have different masses. In a perfect vacuum, this results in the formation of a plasma plume with the lighter particles (with higher speed due to smaller mass) being grouped towards the front of the plasma plume [19].

Higher pressures affect the propagation of the plasma plume. They lead to slower propagation of all species and a sharper plasma plume front - therefore to poorer uniformity of growth [19]. The choice of background gas determines the effect of pressure on crystallinity and growth rate of the thin film [28]. If only argon (inert) gas is used, the argon gas would serve as a scattering medium for the plasma plume species, leading to a lower growth rate at higher argon pressures [18]. This may also lead to oxygen deficient thin film due to preferential scattering of lighter elements [28]. High argon pressures would also lower the kinetic impact of the plasma plume species on the surface of the film, which is an important detail if growth takes place on a material with low binding energy, such as graphene [28].

If pure oxygen gas is used, higher pressures should lead to a higher growth rate of gallium oxide films at a given growth temperature [19]. Oxygen gas serves as a contributing process gas in $Ga_2O_3$ growth, facilitating its growth according to the following two equations [19]:

$$2\,\mathrm{Ga\,(g)} + \frac{1}{2}\mathrm{O_2\,(g)} \longrightarrow \mathrm{Ga_2O\ (g)} \tag{3.2}$$

$$\mathrm{Ga_2O\ (g)} + \mathrm{O_2(g)} \longrightarrow \mathrm{Ga_2O_3\,(s)} \tag{3.3}$$

The absence of input oxygen gas limits the growth rate of $\beta$-$Ga_2O_3$ at a given temperature due to $\beta$-$Ga_2O_3$ decomposition into its suboxide [19].

Pulsed Laser Deposition (PLD) is characterised by a high instantaneous flux of precursors (Ga and O ions) generated after each pulse, arriving on the substrate [19]. At low temperatures, the Ga and O species would adsorb on the surface and would lack the kinetic energy necessary for a sufficiently large surface diffusion length [19]. This leads to the inability of the adatoms to diffuse and incorporate at the appropriate site in the crystal lattice [19]. This may result in a high growth rate of disordered (amorphous) 3D $\beta$-$Ga_2O_3$ films. Relatively high temperatures are therefore necessary as they lead to a higher adatom surface diffusion length, and therefore promote layer-by-layer (2D) growth of single-crystalline $\beta$-$Ga_2O_3$ films [29]. At the even higher temperature end, desorption of adatoms becomes favourable, leading to lower surface diffusion

lengths and growth rates [29]. The oxygen pressure in the chamber determines the temperature thresholds for incorporation/adsorption and desorption of adatoms [19]. For instance, the growth of single-crystalline $\beta$-$Ga_2O_3$ films on sapphire substrates requires low oxygen pressure at low temperature, and higher oxygen pressure at higher pressure.

The laser fluence and spot size of the laser beam on the target also play a significant role in the growth of thin films. First, we have the laser fluence. Fluence of the laser is the energy delivered per unit area to the target. The relationship is given by the following equation:

$$F = \frac{E}{A} \tag{3.4}$$

where $F$ represents the laser fluence ($J/cm^2$), $E$ the laser energy (J), and $A$ the area of the laser spot on the target ($cm^2$). The fluence influences how much energy the target surface absorbs during ablation. The fluence of the laser must be above the congruent ablation threshold - the minimum energy needed to remove material stoichiometrically from the target [18]. At fluences below this threshold, the adsorbed energy mostly contributes to target heating and results in little removal of material [18]. Thermal absorption results in non-stoichiometric ablation of material, which is to be avoided [19]. On the other hand, too high a laser fluence can result in the subsurface boiling of particles of the target and the ejection of molten particles from the target (splashing). As explained earlier, this results in rough films with poor crystallinity and, therefore, with poor electrical properties [19].

The laser's spot size influences the fluence ($\frac{E}{A}$). In addition, the cross-sectional area of the resultant plasma plume is heavily dependent on the size and shape of the spot size [19]. The cross-sectional area of the plasma plume increases when the laser spot size decreases [19]. A smaller spot size, therefore, allows for a more uniform film-thickness distribution [19]. The shape of the spot also matters: a rectangular spot produces an anisotropic plasma plume with an elliptical cross-section. Due to the flip-over effect ([18]), the plume expands more strongly in the direction parallel to the short side of the laser spot, while expansion is more confined along the longer dimension of the spot. A relatively small spot size is preferred, as it allows for a sufficiently wide plasma plume - and therefore for better thickness uniformity - and for a sufficiently high fluence for congruent ablation at a fixed laser energy.

Another parameter that influences the growth of thin films is the distance between the target and substrate (TS distance). Since most of the ablated species will be confined within a forward-directed cone towards the substrate, a suitable TS distance must be chosen to optimise the incident flux on the substrate as well as the kinetic energy of the species arriving on the substrate [18]. When the TS distance is too large, the thickness of the resultant film and its growth rate decreases [18], as the incident flux on the substrate is lower. However, if the distance is too small, due to their high kinetic energy, the incoming species may be unable to adsorb on the substrate; instead, they may be back-reflected [18]. Low TS distances therefore lead to low growth rates, poor crystallinity, and are unsuitable for growth on 2D, Van der Waals bonded materials such as graphene [30]. In addition, low TS distances lead to incongruent ablation, due to target heating. In PLD, the TS distance is usually kept fixed at a value optimised by the manufacturers. In this work, a TS distance of 55.5 mm is used.

In general, in crystal growth, there is almost always a tradeoff between growth rate and crystallinity - a balance between film crystallinity and growth rate must be achieved. Higher growth rates often lead to reduced film crystallinity, whereas obtaining highly crystalline films typically

necessitates slower growth or longer deposition time. In addition to parameters such as growth temperature, process pressure and laser fluence, the laser repetition frequency also plays an important role. For instance, it is expected that the precursor deposition flux must not become excessively high, as this may degrade the crystalline quality of the film. [19]. Consequently, all growth parameters must be carefully adjusted and fine-tuned to achieve the perfect balance between growth rate and crystallinity.

# 4 Theory behind Characterisation tools

## 4.1 X-ray Diffraction

X-ray Diffraction (XRD) is an important technique to determine the crystalline phase, lattice parameters, density of dislocations, and preferred orientation of epitaxial films on a substrate [31]. It is a quick, non-destructive, precise and accurate method [31]. User safety must be accounted for when using X-rays for any application, as prolonged exposure can cause great harm [32]. Therefore, it is important for users of XRD to have completed safety training and to follow the necessary safety measures in place [32].

When an incoming X-ray beam is shone on a sample, part of the beam undergoes elastic scattering (diffraction) [32]. For every orientation of a perfect crystal, there exists an infinite set of parallel planes that contain all the lattice points in the crystal, spaced by a characteristic distance, $d_{hkl}$, as shown in Figure 6 [31].

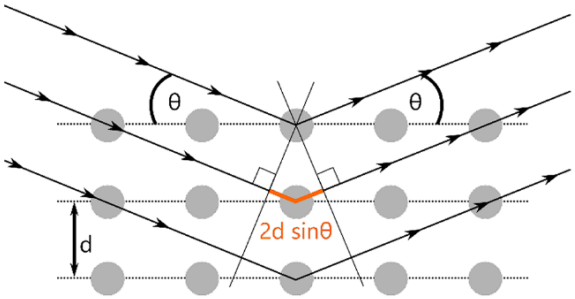


Figure 6: Visualisation of Bragg planes [31].

If the incoming beam is incident at an angle $\theta$ to the horizontal plane, as a result of constructive interference of light reflected from the neighboring planes, and as a consequence of crystalline long range order, a diffraction peak will be observed by the detector only at those angles $\theta$ for which Bragg's condition for diffraction is fulfilled ($\theta_B$) [32]:

$$n\lambda = 2\ d_{hkl}\ \sin\ \theta_B \tag{4.1}$$

where $n$ is an integer corresponding to the order of diffraction, $\lambda$ the wavelength of the X-ray beam, $d_{hkl}$ the characteristic spacing between atomic planes, and $2\ d_{hkl} \sin\theta_B$ is the phase difference between the incoming and scattered rays [31].

The XRD setup has 5 main components: the X-ray source, detector, incident beam optics,

diffracted beam optics and the goniometer (sample stage) [31]. The source produces X-rays within a relatively narrow range of wavelengths that are shone on the sample. The Charged Coupled Detector (CCD) collects and counts the diffracted X-ray photons [31]. The goniometer controls the orientation of the sample (in $\Phi$, $\omega$, $\Psi$) as shown in Figure 7.

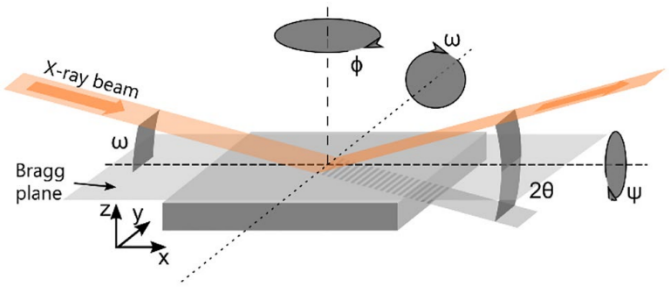


Figure 7: Schematic of degrees of freedom of an XRD goniometer [31].

On the other hand, we have the optics that control the wavelength and divergence of the beam. The type of optics used depends on the type of measurement that needs to be carried out [31]. The two main types of optics in a modern XRD machine are the Bragg-Brentano and Parallel Beam optics. [31].

Bragg-Brentano optics consists of a 4-bounce monochromator placed in front of the source to define a sharp beam wavelength, an opening slit that is placed after the monochromator to reduce the divergence of the beam, and a receiving slit in front of the detector [31]. Bragg-Betano optics provides for high resolution measurements but at low intensity [31]. Parallel Beam optics transforms the divergent beam into a parallel one using a laterally graded multilayer parabolic mirror [31]. Soller slits, which reduce the divergence of the beam, incident and receiving slits, and an axial slit, which determines the size of the main beam, are also used in this set of optics [31]. This method provides for higher intensity, at the expense of resolution [31]. Bragg-Brentano optics is used in this thesis work, as high resolution measurements are necessary.

Two types of commonly performed XRD scans include:
a) $2\theta/\omega$ scan: Here, $\omega$=$\theta$ and $\Psi = 0$, if there is no systemic offset in the orientation of the film Bragg planes with the plane of the substrate. The detector and source are both moved in unison, to vary the angle $\theta$ over a sufficiently large range (e.g. 10° to 90°) [31]. Bragg peaks will be observed only at those angles $\theta_B$ at which Bragg's condition for diffraction is fulfilled. If the Bragg planes of the film are oriented predominantly in a single orientation (e.g. $\bar{2}01$), the film is referred to as single-crystalline [32]. Only higher-order (integer multiples) corresponding Bragg peaks, belonging to the same family of peaks, will be observed [32]. Otherwise, the film is polycrystalline, or if no Bragg peaks are observed, then the film is amorphous [32]. $2\theta/\omega$ scans are therefore vital to determining the preferred orientation of a film on a substrate.

b) $\omega$-scan ("rocking curve"): Here, the angle of the source and detector relative to the plane of the sample is fixed at a value of $\theta$ that satisfies Bragg's condition for diffraction ($\theta_B$), while the sample is oscillated or "rocked" within a small range in $\omega$ [31]. In a perfectly periodic crystal, the Bragg peaks would be delta functions of intensity at angles $\theta_B$; however, in practice, they are broadened [32]. In a low-defect density crystal, instrumental broadening becomes important (e.g., the wavelength is never infinitesimally sharp). In higher defect density crystals, extended defects (dislocations) are mainly responsible for the broadening of the Bragg peaks [32]. Dislocations introduce perturbations to the lattice order, leading to the formation of misaligned "blocks" in the crystal, within which the Bragg planes are aligned well [31]. Therefore,

the Bragg condition for diffraction becomes less stringent on $\theta$, and thus, the diffraction peaks broaden. The larger the Full Width at Half Maximum (FWHM) of the Bragg peak obtained in a $\omega$-scan ("rocking curve"), the greater the dislocation density, and therefore the poorer the crystallinity. The smaller the FWHM, the lower the dislocation density, indicating a better crystallinity film [31].


(a) (b)

Figure 8: (a) XRD setup used for structural characterisation of the thin films in this thesis work, (b) Example of rocking curve scan which gives crystallinity of film.

Figure 8 shows the X-ray diffraction setup used to determine the degree of crystallinity and preferred orientation of the grown films. The labelled parts are as follows, A: X-ray source, B: Goniometer (holds and controls the orientation of the film during XRD measurements with $\Phi$ and $\Psi$ degrees of freedom), C: X-ray detector (to detect the diffracted X-rays).

## 4.2 Scanning Electron Microscopy

Scanning Electron Microscopy (SEM) is a technique that is convenient to characterise the surface morphology of thin films across relatively large areas (above 20 x 20 µm). SEM works via the application of a focused beam of high-energy electrons across the surface of the sample [33]. An SEM is made up of several components that include an electron gun, beam apertures, scanning coils, sample stage, detectors, electron lenses and display output [34] [33]. The electron gun produces electrons that are accelerated via the application of a high voltage (10-25 kV), and then focused to a spot on the surface of the film [34].

The elastic and inelastic interactions between the electrons and the sample are responsible for the generation of multiple signals that provide compositional and topographical surface information [33]. The signals involve backscattered electrons, elastically reflected electrons, secondary electrons and characteristic X-ray photons [34]. Backscattered electrons (BSE) are electrons from the original beam that have been elastically scattered by the nuclei of the sample [34]. As a result, BSEs provide compositional contrast; e.g., denser materials generate a greater number of BSEs relative to less dense materials (or those with a smaller atomic number). Secondary electrons (SE) are electrons generated from the sample, following inelastic interactions of the sample with the incoming electron beam [33]. They have low energies (~50 eV), and thus can only originate from the surface of the sample (from a depth of 5-50 nm) [33]. Therefore, they provide topographical contrast to an excellent resolution (5-10 nm, depending on the voltage).

These resultant signals are collected by the relevant detectors to produce the SEM images. A SEM setup is easy to use, provides rapid data acquisition, and if the relevant detector is present, also provides the ability to determine the chemical composition of the sample via Energy-Dispersive X-ray Spectroscopy (EDS) [35]. Inelastic interactions between beam elec-

trons and the sample may lead to the ejection of core electrons from sample atoms. Following de-excitation of the atoms via transitions of electrons from the outer to the vacant inner electronic shells, X-ray photons with energy equal to the energetic difference between the two shells involved are emitted and collected by a detector [35]. Analysing the energies of the photons provides a direct way to identify the chemical composition of the sample, as each atom has a unique electronic configuration and ground state, and the emitted photons are then characteristic of the elements that are present in the sample [35]. This is crucial to determine if the grown thin film is, in fact, gallium oxide. The EDS software separates the characteristic X-rays from different elements present in the sample, generating an energy spectrum [35]. The spectrum is automatically analysed to fit for the atomic percentage of each element in the sample [35]. Compositional elemental maps can also be generated.

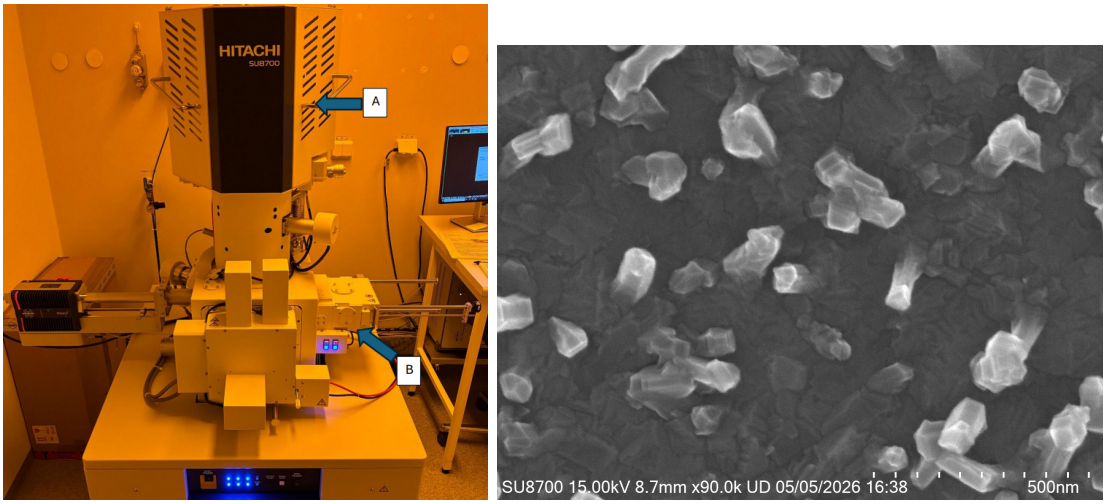


(a) (b)

Figure 9: (a) Scanning Electron Microscope used for the characterisation of thin films in this thesis work. (b) Example of a characterisation image taken which gives us surface morphology of a film's surface.

Figure 9 (a) shows the scanning electron microscope that was used for this thesis work. The labelled components are as follows, A: Electron gun (used to produce and accelerate electrons for microscopy), B: Specimen Exchange Chamber (Used to load and unload samples into the SEM for analysis). Figure 9 (b) shows an example of a resultant SEM image of a film.

### 4.3 Spectroscopic Ellipsometry

Spectroscopy ellipsometry is an optical characterisation technique for thin films. It provides a non-destructive and indirect method for the determination of film thickness and dielectric function [36].

In our setup, linearly polarized white light with two polarization components is shone onto the sample: one electric field vector is parallel to the plane of incidence ('p-polarized'), while the second electric field vector is perpendicular to the plane of incidence ('s-polarized'). Linearly polarised light undergoes a change in polarisation upon reflection from a thin film surface on a substrate. The change is described by changes in amplitude ratio between p- and s-polarised reflected light ($\Psi$), in their phase difference ($\Delta$) – these two quantities are measured as a function of wavelength by the detector in spectroscopic ellipsometry. The fundamental ellipsometric equation below is used to infer the film thickness and dielectric function [28]:

$$\tan(\Psi)e^{i\Delta} = \frac{r_p}{r_s} \tag{4.2}$$

where $r_p$ and $r_s$ stand, respectively, for the reflection coefficients of p- and s-polarized light from the sample. The values for these two quantities are computed by the setup's software by solving Maxwell's equations for the reflection of light at each interface in the sample [37]. Therefore, an input model for the sample's structure - including film thickness, refractive index and extinction coefficient of each layer in the sample - is necessary for their computation.

In our case, the structure of our samples is modelled as air-gallium oxide-SiC. To model the refractive index and absorption coefficient of $\beta$-$Ga_2O_3$ and SiC, we have used the Cauchy model. The Cauchy model is appropriate for modelling the dielectric function of (transparent) wide bandgap materials [36]. In this model, the refractive index as a function of wavelength is given by [36]:

$$n(\lambda) = A + \frac{B}{\lambda^2} + \frac{C}{\lambda^4} \tag{4.3}$$

where A, B, and C are empirical fitting parameters. The extinction coefficient (k) is modelled by the function [38]:

$$k(\lambda) = k_{\text{amp}}\, e^{\beta\left(\frac{1.24}{\lambda} - \frac{1.24}{\lambda_{\text{BE}}}\right)} \tag{4.4}$$

where $k_{\text{amp}}$ and $\beta$ are fit parameters, and $\lambda_{\text{BE}}$ is the band edge (380 nm for 4H-SiC, and 253 nm for $\beta$-$Ga_2O_3$ [14]). The overall model for the sample is then inputed into the ellipsometry fitting software, which computes and plots the theoretical values of $\Psi$ and $\Delta$ on the basis of the model. The fitting parameters are varied until the theoretical values are a good fit to the observed values. This is done in an iterative manner until the mean square error (MSE) of the fitting - the square root of the sum of the differences in numerical values between the theoretical and experimental values - is minimized [36]. The film thickness is then noted down.

Figure 10 (a) shows the spectroscopic ellipsometer that is used to determine the thickness of thin films in this thesis work and its schematic. The specific parts of this tool can be described as the following, A: Light source (produces linearly polarized white light), B: Detector (used to detect the change in the polarisation of the reflected light), C: Sample stage (used to hold the substrate during measurements). Figure 10 (b) shows the schematic diagram of the double polarised light and its components.

## 4.4 Reflection High-Energy Electron Diffraction

Reflection High-Energy Electron Diffraction (RHEED) is a widely used technique for monitoring the epitaxial growth of thin films [40]. One of its major advantages is that it enables characterisation of thin-film surface without interrupting the growth process [40]. In RHEED, a focused beam of high-energy electrons is directed onto the sample's surface at a very small grazing incident angle, typically only a few degrees [41]. Due to this shallow incident angle, the electrons penetrate only the topmost atomic layers of the film, making RHEED highly surface

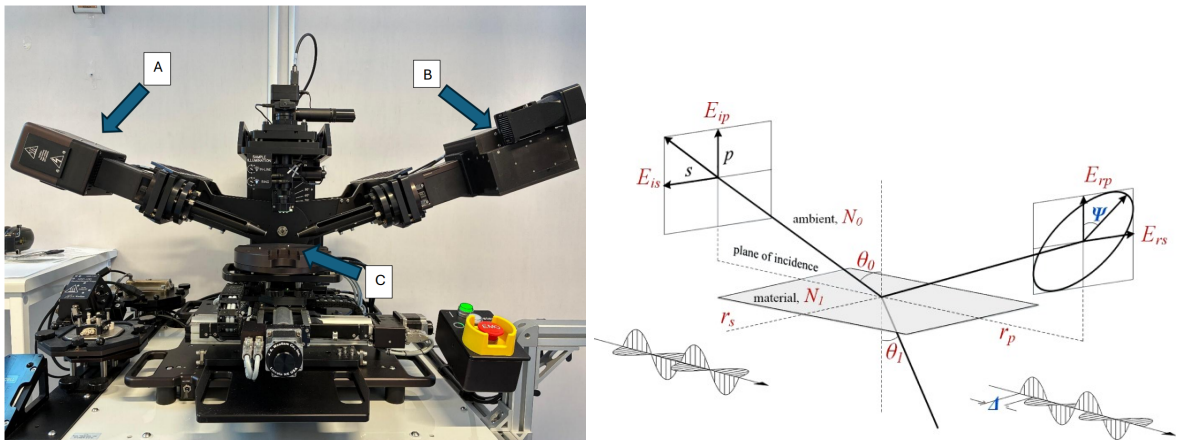


(a) (b)

Figure 10: (a) Spectroscopic Ellipsometer used for characterisation of thin films in this thesis work. (b) Schematic of spectroscopic ellipsometry [39].

sensitive. The electrons scatter elastically from the periodic arrangement of surface atoms, producing diffraction patterns that encode information about surface structure, morphology, and crystalline quality of the growing film [41].

RHEED systems are made up of an electron gun and a detector, most commonly a phosphor screen coupled to a camera for image acquisition [40]. The electron beam is generated by a very thin filament. Apertures, focusing lenses and deflection coils are used to control the beam size and trajectory [40][41] . The resulting RHEED pattern observed arises from constructive interference of elastically scattered electrons from the periodic surface (2D) lattice [41].

Thanks to the surface-sensitivity of RHEED, the diffraction pattern can be used to identify the growth mode of the film *in situ* [40]. For smooth 2D (FVDM) growth, the RHEED pattern consists of sharp streaks, indicating a flat and well-ordered surface. In contrast, 3D island growth (VW) produces spotty diffraction features due to transmission-like diffraction through the islands [41]. Amorphous films produce diffuse patterns because of the lack of long-range surface crystalline order. Consequently, RHEED provides a rapid, *in situ* method for determining whether crystalline growth is occurring during deposition.

In this thesis, the evolution of the RHEED pattern *in situ* is monitored to determine the completion of the nucleation layer during heteroepitaxial PLD growth. In heteroepitaxial growth, the nucleation layer is a transitional layer between the substrate and the epitaxial film, which accommodates lattice and structural mismatches during the early stages of growth [42]. At the beginning of deposition, the nucleation layer is initially amorphous or poorly crystalline and therefore does not produce a distinct RHEED diffraction pattern [41] [42]. As deposition continues, the nucleation layer gradually crystallises and develops sufficient long-range order for diffraction to occur [40]. The appearance of a clear RHEED pattern, therefore, indicates the formation of a crystalline nucleation layer and marks the transition from amorphous to crystalline growth.

## 4.5 Atomic Force Microscopy

Atomic Force Microscopy (AFM) is used in this thesis to characterise the surface topography of the thin films. Compared to SEM, AFM provides direct three-dimensional surface height information with sub-nanometre vertical resolution, making it particularly suitable for quantitative

surface roughness and morphology analysis [43].

AFM employs a sharp nanoscale tip that scans across a small area of the sample surface to generate a high-resolution topographic map [43]. AFM operates by measuring the interaction forces between the atoms at the tip's apex and the sample surface. Depending on the tip-sample separation, these interactions include attractive Van der Waals forces or short-range repulsive forces arising from overlapping electron orbitals [44]. The tip is mounted on a flexible cantilever whose vertical position is controlled by a feedback loop to maintain a constant interaction between the tip and the surface during scanning [44]. Cantilever deflection is measured using a laser beam reflected onto a photodiode detector, allowing for accurate measurements of the tip-surface distance, and therefore for precise determination of the surface morphology [44].

AFM can operate in contact, non-contact, and tapping modes [44]. In contact mode, the tip remains in physical contact with the surface, which can lead to tip wear or sample damage [44]. In non-contact mode, the cantilever oscillates near its resonance frequency while the tip remains slightly above the surface, probing attractive forces without physical contact. Although this mode provides very high vertical resolution, it generally requires slow scan speeds and carefully controlled conditions [44].

In this thesis, tapping mode AFM is used. In this mode, the cantilever oscillates with an amplitude of several tens of nanometres, intermittently contacting the sample surface during scanning [44]. This reduces lateral forces and minimises tip-induced damage while maintaining high spatial resolution [43]. A Bruker AFM operated in tapping mode with a lateral resolution of 5 nm and a vertical resolution of 0.5 nm is used in this work.

# 5 Methods

The PLD system used in this work employs a KrF (krypton-fluoride) excimer laser with a wavelength of 248 nm, placing it in the ultraviolet spectral region. Stimulated emission from the KrF excited dimers ('excimers') is generated using a discharge voltage of 22kV, which was selected to provide optimal pulse-to-pulse energy stability. The emitted laser beam is circular, 2-inch in diameter. To obtain a spatially homogeneous beam profile, a rectangular aperture with dimensions 4.1 mm x 15.1 mm is placed in front of the laser output, allowing only the portion of the beam with uniform energy to pass through. The rectangular beam is then focused onto the target using a UV lens with a focal length of 452.73 mm. Using aperture-lens and lens-target distances of 3887.7 mm and 512.4 mm, respectively, the optical system produces a rectangular laser spot on the target with dimensions 0.84 mm x 1.99 mm, corresponding to an area of 1.67 $mm^2$. This laser spot size was kept constant throughout all growth experiments.

The laser fluence was initially increased from low values until the threshold for congruent ablation was identified. This threshold was determined to be approximately 1.50 $J/cm^2$, by analysing the film stoichiometry using EDS, as shown in Figure A.3 in the Appendix. When the measured Ga:O atomic ratio approached the stoichiometric ratio of 2:3 for $Ga_2O_3$, the ablation process was considered congruent. Following this optimisation, most growths were performed at a laser fluence of 1.68 $J/cm^2$.

Silicon carbide (SiC) was selected as the substrate material due to its relatively lower cost,

high thermal conductivity, ability to support epitaxial graphene growth through Si sublimation, and comparatively small lattice mismatch with $\beta$-$Ga_2O_3$. The substrates used were c-plane (001)-oriented 4H-SiC with dimensions of 1.0 cm × 1.0 cm.

Prior to growth, the SiC substrates were cleaned sequentially in acetone, isopropyl alcohol (IPA), and deionised (DI) water using an ultrasonic bath for 5 minutes in each solution to remove organic contaminants. To promote reproducible epitaxial growth, consistent target surface conditions between depositions must be maintained. For this reason, the target was polished and pre-ablated before each growth run. Pre-ablation was performed under vacuum across the entire 2-inch target surface using a total of 1500 laser pulses. The target was raster-scanned at speeds of 0.5 mm/s and 2 mm/s, in x and y directions, respectively. The same laser fluence and repetition rate used during film growth were also used during the pre-ablation process.

The growth parameters were systematically varied, one at a time, to investigate their influence on growth rate and crystalline quality. The primary parameters studied were the substrate temperature and oxygen background pressure during growth. Figure 11 shows the matrix of growth temperatures and oxygen pressures investigated, together with the corresponding growth runs. Table 2 lists the parameters kept constant for this matrix. During these experiments, the laser fluence was kept constant at 1.68 J/cm$^2$. The TS distance was fixed at the manufacturer-optimised value of 55.5 mm, while the laser repetition rate was maintained at a conservative value of 2 Hz for these growth runs. In addition, the number of laser pulses was kept constant at 5000 pulses per deposition to ensure consistency between experiments.

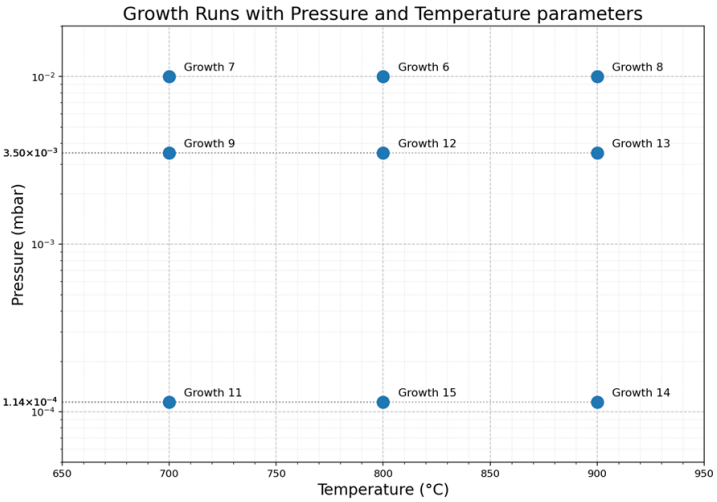


Figure 11: Plot of growth parameters for the pressure and temperature matrix according to growth run.

Upon completion of the inital growth matrix, all deposited thin films were characterised using XRD, spectroscopic ellipsomtery and SEM. Based on the structural, morphological, and optical characterisation results, the film exhibiting the best balance between growth rate and crystal quality was selected for further process optimisation. In the next growth run (Growth 16) a low-temperature gallium oxide buffer layer was introduced prior to the main film deposition. The buffer layer was grown in an argon atmosphere to suppress oxidation of the SiC surface that can occur upon direct exposure to oxygen during high-temperature growth, with the aim of improving the crystalline quality of the subsequently deposited film. The buffer layer was deposited at 700°C in 1x10$^{-2}$ mbar argon using 1700 pulses. RHEED was used to monitor the crystallization of the buffer layer and determine the minimum number of pulses required for formation of a crystalline nucleation layer (Figure A.5). The growth conditions for the buffer

| Growth | Temp. (°C) | Pressure (mbar) | Process Gas | Fluence (J/cm$^2$) | Freq. (Hz) | Buffer pulses | Film pulses |
|---|---|---|---|---|---|---|---|
| 1 | 800 | 0.01 | $O_2$ | 1.10 | 2 | - | 5000 |
| 2 | 800 | 0.01 | $O_2$ | 1.20 | 2 | - | 5000 |
| 3 | 800 | 0.01 | $O_2$ | 1.30 | 2 | - | 5000 |
| 4 | 800 | 0.01 | $O_2$ | 1.40 | 2 | - | 5000 |
| 5 | 800 | 0.01 | $O_2$ | 1.50 | 2 | - | 5000 |
| 6 | 800 | 0.01 | $O_2$ | 1.68 | 2 | - | 5000 |
| 7 | 700 | 0.01 | $O_2$ | 1.68 | 2 | - | 5000 |
| 8 | 900 | 0.01 | $O_2$ | 1.68 | 2 | - | 5000 |
| 9 | 700 | 0.0035 | $O_2$ | 1.68 | 2 | - | 5000 |
| 11 | 700 | 0.00014 | $O_2$ | 1.68 | 2 | - | 5000 |
| 12 | 800 | 0.0035 | $O_2$ | 1.68 | 2 | - | 5000 |
| 13 | 900 | 0.0035 | $O_2$ | 1.68 | 2 | - | 5000 |
| 14 | 900 | 0.00014 | $O_2$ | 1.68 | 2 | - | 5000 |
| 15 | 800 | 0.00014 | $O_2$ | 1.68 | 2 | - | 5000 |
| 16 | 800 | 0.01 | $O_2$, Ar | 1.68 | 2 | 1700 | 3300 |
| 17 | 800 | 0.01 | $O_2$, Ar | 1.38 | 2 | 1700 | 3300 |
| 18 | 800 | 0.01 | $O_2$, Ar | 1.98 | 2 | 1700 | 3300 |
| 19 | 800 | 0.01 | $O_2$, Ar | 1.98 | 3 | 1700 | 3300 |
| 20 | 800 | 0.01 | $O_2$, Ar | 1.98 | 5 | 1700 | 3300 |
| 21 | 800 | 0.01 | $O_2$, Ar | 1.98 | 2 | 5000 | 5000 |

Table 1: Growth conditions of every run conducted in this thesis work.

| Laser Fluence (J/cm$^2$) | TS distance (mm) | Laser Frequency (Hz) | Pulse length |
|---|---|---|---|
| 1.68 | 55.5 | 2 | 5000 |

Table 2: Parameters kept constant for temperature and pressure matrix growth runs.

layer were kept constant for all subsequent growths in which the laser fluence and repetition rate were varied (Growths 16-20). In each case, the main $\beta$-$Ga_2O_3$ layer was grown using the optimised conditions identified from Growth 6. The thin film was then grown with the best yielding parameters from the matrix, which came from growth run 6 (i.e., 800 °C and the oxygen pressure at 1x10$^{-2}$ mbar).

The next parameter investigated was the laser fluence, which was varied by ±0.30 J/cm$^2$ around 1.68 J/cm$^2$. Tables 3 and 4 show the growth conditions for growth runs 16-18, which were grown with the same buffer layer process. After deposition, the films were again characterised using XRD, SEM, and spectroscopic ellipsometry. From these experiments, the best film quality and growth rate was obtained at a laser fluence of 1.98 J/cm$^2$, corresponding to Growth 18.

| Laser Fluence (J/cm$^2$) | 1.38 | 1.68 | 1.98 |
|---|---|---|---|
| **Growth Run** | Growth 17 | Growth 16 | Growth 18 |

Table 3: Matrix of laser fluence corresponding to growth run.

| Temperature (°C) | TS distance (mm) | Laser Frequency (Hz) | Pressure (mbar) |
|---|---|---|---|
| 700 - 800 | 55.5 | 2 | 1x10$^{-2}$ |

Table 4: Parameters kept constant for laser energy matrix growth runs.

The laser repetition rate was then varied, while all other parameters were kept constant. The growth runs and growth conditions corresponding to this series are listed in the two tables below (Tables 5 and 6):

Finally, the last growth run, Growth 21, was conducted using a thicker buffer layer consisting of 5000 pulses. All other growth parameters were chosen based on the previously optimised conditions. The buffer layer was grown at 700°C in 1x10$^{-2}$ mbar argon pressure, while the main

| **Laser Frequency (Hz)** | 2 | 3 | 5 |
|---|---|---|---|
| **Growth Run** | Growth 18 | Growth 19 | Growth 20 |

Table 5: Matrix of laser fluence corresponding to growth run.

| **Temperature (°C)** | **TS distance (mm)** | **Laser Fluence (J/cm$^2$)** | **Pressure (mbar)** |
|---|---|---|---|
| 700 - 800 | 55.5 | 1.98 | 1x10$^{-2}$ |

Table 6: Parameters kept constant for Laser Frequency matrix growth runs.

film was grown at a substrate temperature of 800°C and an oxygen pressure of 1x10$^{-2}$ mbar. Additional growth parameters included a TS distance of 55.5 mm, a laser fluence of 1.98 J/cm$^2$, a laser frequency of 2 Hz, and 5000 pulses for the main film deposition. The resulting film was characterised using SEM, XRD, spectroscopic ellipsometry, and AFM.

For all growth runs, XRD measurements consisting of $2\theta/\omega$ scans and rocking curve measurements were performed. The Full Width at Half Maximum (FWHM) of the rocking curves was determined by applying Gaussian fits using Python.

After deposition, all samples were cooled from the growth temperature under the same oxygen pressure used during deposition. Cooling was continued until the heater temperature reached 300°C. Figure 12 shows a flowchart of every step taken in each growth run during this thesis work.

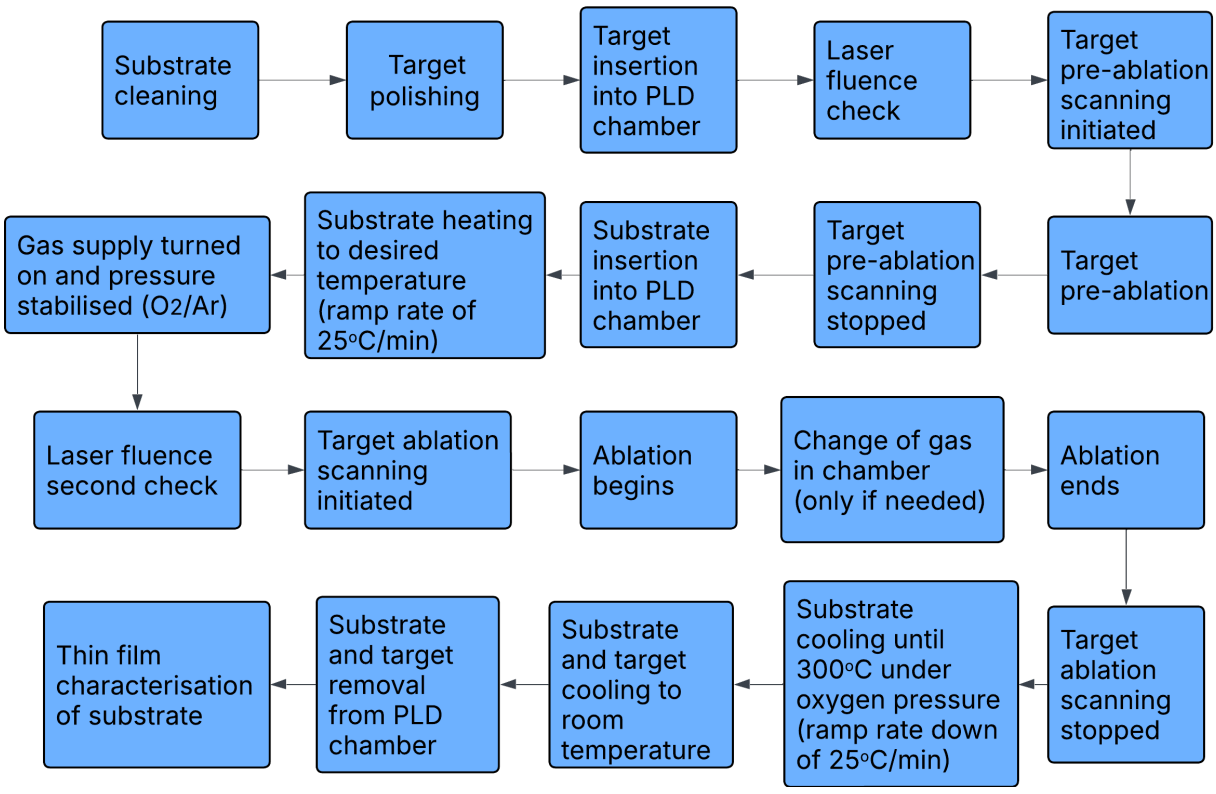


Figure 12: Flowchart of steps taken during each growth run.

# 6 Results and Discussion

## 6.1 Growth Rates

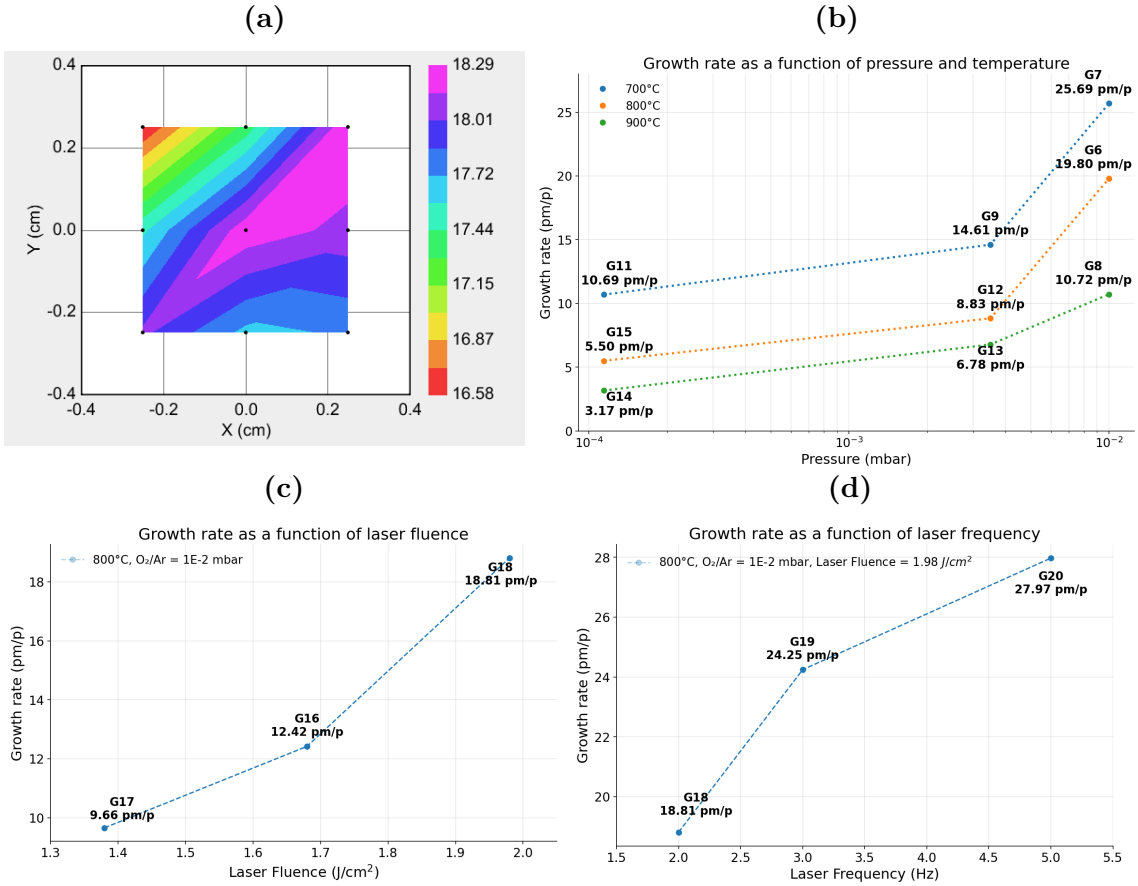


Figure 13: (a) Thickness map of film in Growth 6. Growth rate in picometer/pulse (pm/p) based on: (b) pressure and temperature, (c) laser fluence, (d) laser frequency.

Figure 13 (a), shows the thickness distribution map for Growth 6, determined by spectroscopic ellipsometry, across 9 points within the 4x4 mm rectangular region centered on the sample. The thickness maps for all the growths are shown in Figure A.6 in the Appendix. The same measurement pattern was used for all samples, and the average film thickness for each growth was extracted (Table A.1 in the Appendix). These average thicknesses were subsequently used to calculate the growth rate in picometres per pulse for each sample (Table A.1 in Appendix).

Figure 13 (b) presents the growth rates of all the samples in the oxygen pressure -temperature growth matrix. At a fixed oxygen pressure, the growth rate decreases with increasing growth temperature – a trend that is consistently observed for all three oxygen pressures investigated. At a fixed oxygen pressure, higher growth temperatures promote the desorption of adatoms from the $Ga_2O_3$ surface, thereby reducing the growth rate. Equivalently, this behaviour can be interpreted thermodynamically as Equation 3.3 increasingly proceeding in the reverse direction: the formation of crystalline $Ga_2O_3$ becomes less favourable, while its decomposition into $Ga_2O$ (g) and $O_2$ (g) is enhanced.

On the other hand, at any given fixed growth temperature, increasing the oxygen pressure leads to higher growth rates. A higher oxygen input favours the thermodynamics of $Ga_2O_3$ crystal growth (Eq 3.3), suppressing decomposition and thereby shifting the onset of adatom

desorption to higher temperatures. The observed trends suggest that higher oxygen pressures, therefore, enable the growth of $Ga_2O_3$ at higher substrate temperatures.

Figure 13 (c) and (d) show the dependence of growth rate on laser fluence and repetition rate, respectively. The observed increase in growth rate with fluence is consistent with the increase in instantaneous flux of gallium- and oxygen-containing species generated during each pulse. The increase in the growth rate per pulse with pulse frequency is an interesting result that suggests an increase in incorporation efficiency. It is possible that the increased time-averaged flux at higher pulse frequencies may suppress decomposition by reducing the effective rate of adatom desorption from the surface. At higher pulse frequencies, the surface may reach a steady state condition in which adatom loss between pulses is reduced, leading to a greater net incorporation per pulse.

It is noteworthy that Growth 16 exhibited a lower growth rate than Growth 6. The only difference between these two growths was that, for Growth 16, a thin buffer layer was first deposited in argon for 1700 pulses before the growth of the main film in oxygen for 3300 pulses. This approach was used to suppress the formation of an amorphous interfacial layer arising from the oxidation of Si species in the SiC substrate. The successful growth of gallium oxide under zero (excess) oxygen input during the buffer-layer stage demonstrates the ability of PLD to achieve stoichiometric transfer from target to film. The reduced growth rate is expected, since argon acts only as an inert scattering medium for the gallium- and oxygen-containing species, and does not participate chemically in the growth process. The scattering reduces the net precursor flux arriving at the substrate, thereby reducing the growth rate.

## 6.2 Structural and Morphological Properties of the Grown Films

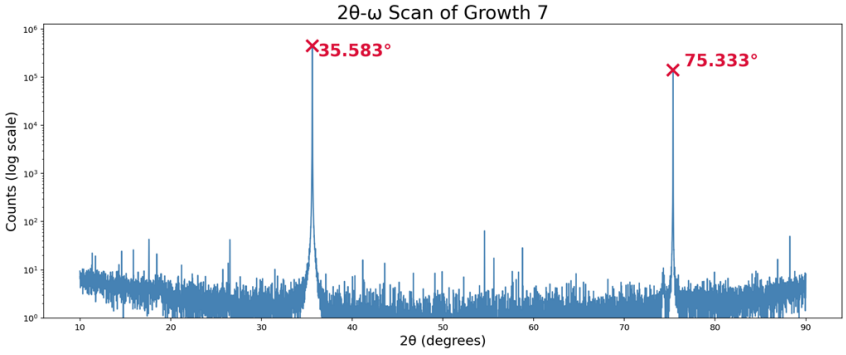


(a)

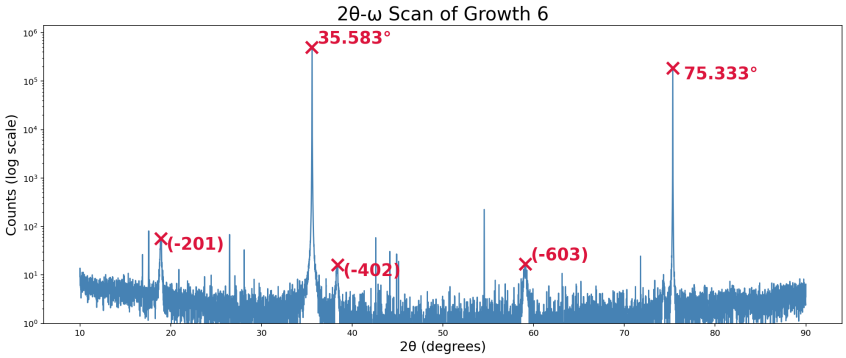


(b)

Figure 14: (a) $2\theta/\omega$ scan plot of Growth 7. (b) $2\theta/\omega$ scan plot of Growth 6.

Figure 14 (a) shows the $2\theta/\omega$ XRD scan for Growth 7 over the angular range of 10°-90° in $2\theta$. Bragg peaks occur at 35.583°± 0.009°, and 75.333°± 0.005° peaks, corresponding to the

(004) and (008) Bragg reflections of the 4H-SiC substrate [45], respectively. No Bragg peaks associated with gallium oxide are observed. Given that the film thickness is approximately 124 nm (Table A.1), the film is sufficiently thick to provide a measurable X-ray scattering volume. The absence of gallium oxide diffraction peaks therefore indicates that the film is amorphous; i.e., the gallium oxide domains possess no preferred crystallographic orientation, but are instead randomly oriented.

The relatively high oxygen pressure (0.02 mbar) and low temperature (700° Celsius) favour the thermodynamics of $Ga_2O_3$ growth, resulting in efficient incorporation of the adatoms into the film, and therefore to the high growth rate observed. However, at this temperature, the surface diffusion length of the adatoms remains limited, inhibiting long-range crystalline ordering. The result is the growth of a structurally disordered film consisting of small, randomly oriented crystallites, as seen in Figure 16 (a) and Figure 17 (a).

The absence of gallium oxide Bragg peaks in $2\theta/\omega$ is also observed for Growths 13 and 14- These films were grown at high temperature (900°C) and low oxygen pressure (below 0.01 mbar) – conditions which promote desorption of adatoms from the surface over their incorporation, leading to lower surface diffusion length, and therefore poorer crystallinity and lower growth rate.

Figure 14 (b) shows a $2\theta/\omega$ XRD scan for Growth 6, which was grown at the same oxygen pressure as Growth 7, but at a substrate temperature 100° C higher. The presence of the $(\bar{2}01)$, $(\bar{4}02)$, and $(\bar{6}03)$ peaks at 18.911°± 0.001°, 38.332°± 0.003°, and 59.058°± 0.004° respectively, demonstrates the formation of preferentially oriented $\beta-Ga_2O_3$ along the $[\bar{2}01]$ direction. The higher growth temperature increases the surface diffusion length of the adatoms, enabling gallium oxide domains to align preferentially along the $[\bar{2}01]$ direction, and thereby form a single-crystalline, $\beta-Ga_2O_3$ film. This demonstrates that, at a fixed oxygen pressure, higher substrate temperatures are needed for the growth of single-crystalline $\beta-Ga_2O_3$ films.

The remaining growths in the matrix also exhibit a $(\bar{2}01)$ preferential orientation, including growths 9 and 11, which were deposited at the same temperature as Growth 7 – demonstrating that lower oxygen pressures favour the growth of single-crystalline films at low substrate temperatures.

Figure 15 (a) presents the $(\bar{2}01)$ rocking curves for Growth runs 6, 12, and 15. These films were all grown at the same growth temperature of 800°C, but at oxygen pressures of $1\times10^{-2}$ mbar, $3.5\times10^{-3}$ mbar, and $1.14\times10^{-4}$ mbar, respectively, while all the other growth parameters were fixed. The rocking curve FWHM is observed to increase with oxygen pressure at this temperature. At a fixed temperature, lower oxygen pressures lead to lower growth rates, thereby allowing adatoms more time to diffuse across the surface and incorporate at the appropriate lattice sites, resulting in better crystal quality and consequently narrower rocking curves.

The FHWM values of Growth 11 and Growth 9 do not appear to follow this trend (Figure 15 (b)). The origin of this deviation is unclear. Additional growth mechanisms may influence the crystalline quality under these conditions.

Table A.4 lists the FWHM values of the $(\bar{2}01)$ rocking curves for all samples in which this reflection could be observed. Among the films in the growth matrix, Growth 15 exhibits the highest crystalline quality, with a rocking curve FWHM of approximately 1.674°± 0.189°, but a relatively low growth rate (5.50 pm/p, Table A.1 in the Appendix). In contrast, Growth 6 exhibits the highest growth rate (among crystalline films) in the matrix (19.8 pm/p), but with a FWHM approximately 1.5 times larger than that of Growth 15. *In situ* RHEED measurements during growth 6 revealed the formation of an amorphous interfacial layer during approximately

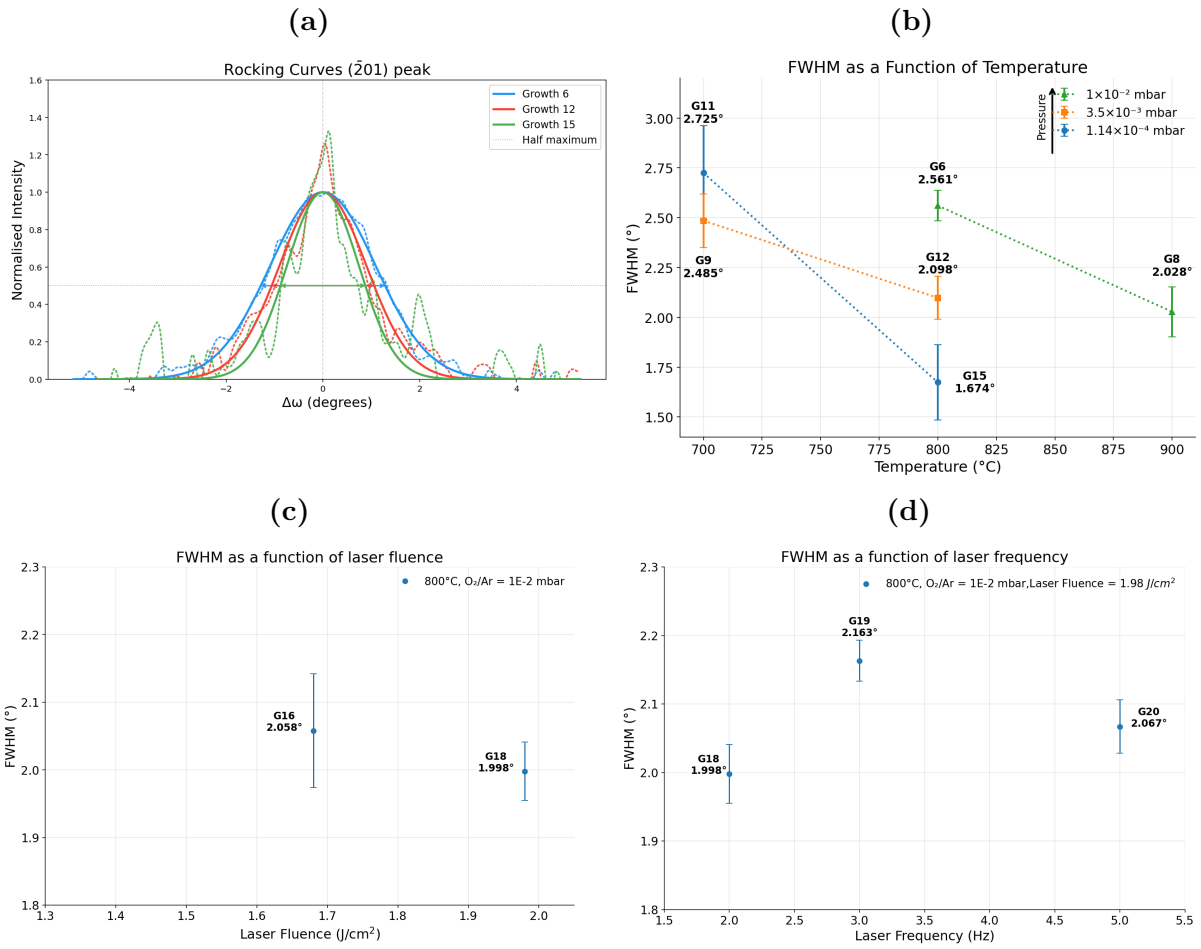


Figure 15: (a) Combined FWHM Gaussian Fits for Growth runs at fixed temperature (800 °C). FWHM trends under different growth parameters: (b) pressure dependence, (c) laser fluence dependence, (d) laser frequency dependence.

the first 15 minutes of growth. After 15 minutes, reciprocal lattice rods began to develop in the RHEED pattern, consistent with the onset of crystalline gallium oxide growth via the (FVDM) growth mode. However, the rods remained broad and of relatively low intensity, hinting at poor crystallinity (Figures A.4 in the Appendix).

A plausible explanation is that direct exposure of the bare SiC substrate to oxygen during the initial growth stage promotes oxidation of the SiC surface, resulting in the formation of an amorphous interfacial oxide layer. Such a disordered interfacial layer provides a structurally poor template for subsequent epitaxial growth of gallium oxide – consistent with the weak and broad reciprocal lattice rods observed by RHEED.

To suppress the oxidation of the SiC surface and thereby improve the crystallinity quality under the Growth 6 conditions, a modified growth procedure was implemented for the next growth (Growth 16). In this case, a thin low-temperature gallium oxide buffer layer was first deposited in argon at 700°C and 0.01 mbar for 1700 pulses, before the growth of the main film in oxygen for 3300 pulses under the same growth conditions as Growth 6. RHEED measurements were used to determine the number of pulses needed to complete the formation of a high crystal quality nucleation layer. Sharp reciprocal lattice rods, shown in Figure A.5 (a) in the Appendix, indicated that approximately 1700 pulses were sufficient to establish a high crystal quality buffer. Although this modified growth sequence reduced the overall growth rate by 36% relative to

Growth 6 (from 19.80 pm/p to 12.42 pm/p), the crystalline quality improved significantly, with the rocking curve FWHM decreasing by approximately 20% to 2.067°± 0.039° from 2.561°± 0.076°.

Given that sample Growth 16 provided the best compromise between growth rate and crystal quality, the subsequent series focused on investigating the role of fluence. The fluence was varied by ±0.30 J/cm$^2$ around the baseline value of 1.68 J/cm$^2$, while all other growth conditions were kept identical to those of Growth 16.

Growth 17, deposited at a fluence of 1.38 J/cm$^2$, was found to be amorphous. This is consistent with the fluence lying below the threshold required for congruent ablation of the target material (1.5 J/cm$^2$). Figure 15 (c) shows that the rocking curves FWHM values of Growths 16 and 18 are very similar, with values of 2.058°± 0.084° and 1.998°± 0.043° respectively, despite the increase in fluence from 1.68 J/cm$^2$ to 1.98 J/cm$^2$. This trend suggests that, within this fluence range, the crystalline quality is relatively insensitive to fluence (above the threshold for congruent ablation). Additional data points are required to establish a definite trend. In contrast, the growth rate increased significantly, improving by nearly 50% relative to Growth 16 and reaching 18.81 pm/p for Growth 18.

In an attempt to further increase the growth rate, two additional growth runs were conducted at pulse frequencies of 3 Hz and 5 Hz, while otherwise maintaining the same growth conditions as Growth 18. As shown by the three data points in Figure 15 (d), the FHWM of the ($\bar{2}$01) rocking curve appears to increase with pulse frequency, consistent with a reduction in crystalline quality at higher time-averaged precursor flux. However, as with the fluence series, more than three data points are necessary to conclude on a trend.

The growth rates of the films grown at pulse frequencies above 2 Hz were at least 29% higher than that of Growth 18. However, SEM imaging (Figure 16 (c)) revealed significantly rougher surface morphologies for these films (Growth 20), likely arising from the increased time-averaged precursor flux arriving at the substrate surface. Such rough surface morphologies are undesirable, as they are expected to degrade the electrical properties of the films [11].

In an attempt to further improve the crystallinity under the Growth 18 conditions, an additional sample (Growth 21) was deposited using identical growth conditions but with a thicker buffer layer grown for 5000 pulses. This resulted in a 108.07 nm thick film, with a significantly improved ($\bar{2}$01) rocking curve FWHM of 1.627°± 0.034°. This improvement is consistent with the established understanding of heteroepitaxial growth, where the density of dislocations in heteroepitaxial films decreases with increasing buffer layer thickness. A thicker buffer layer can confine more efficiently or terminate dislocations arising from lattice mismatch before they propagate into the epitaxial film [42]. Figure 17 (b) depicts a 2x2 $\mu$m AFM scan of the surface of Growth 21. The surface is relatively smooth, exhibiting a root-mean-square roughness of 2.5 nm. In addition, the observed domain sizes are considerably larger than those observed for Growth 7 - consistent with enhanced adatom surface diffusion length at the optimised growth conditions.

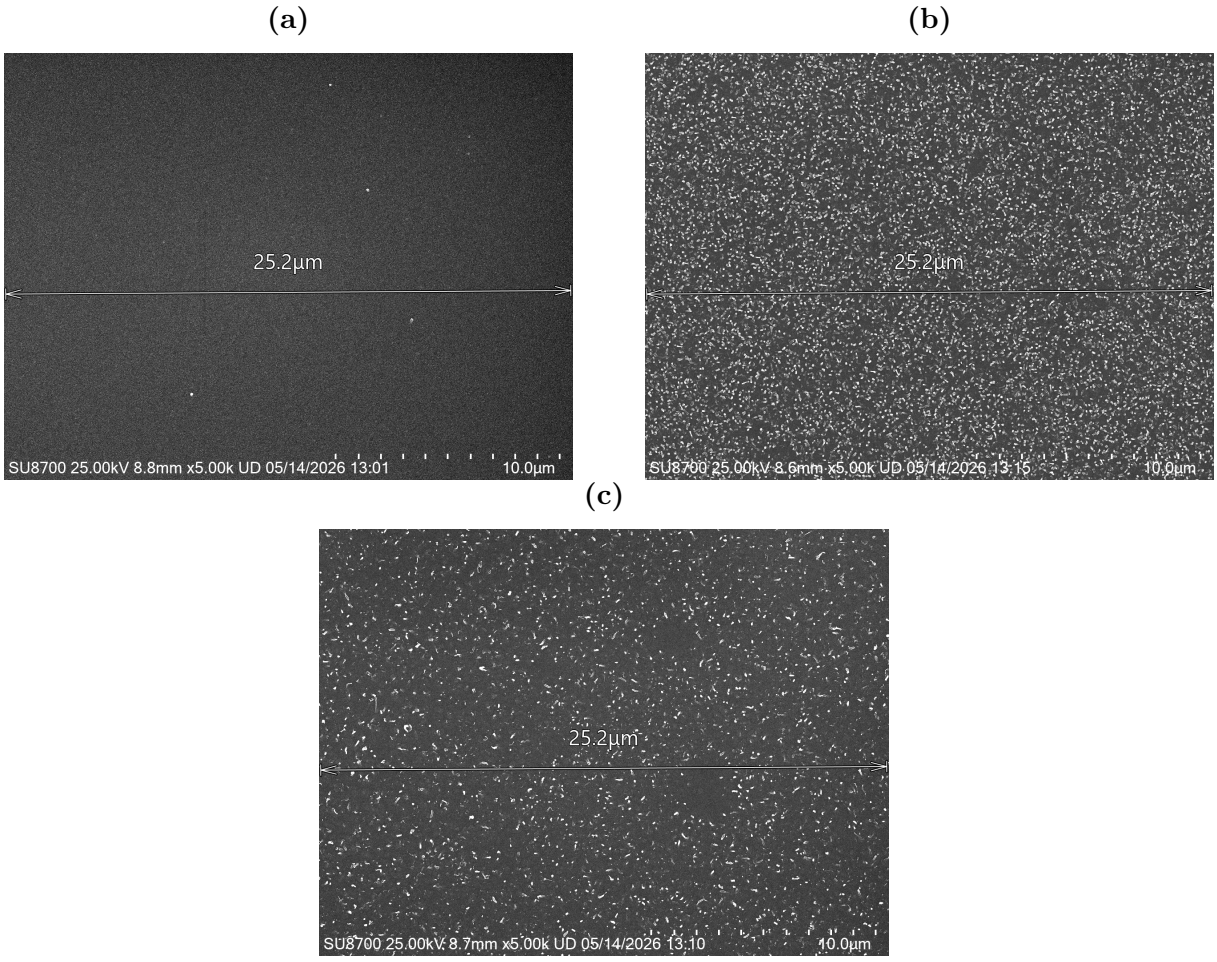


Figure 16: Scanning Electron Microscope images of films from: (a) Growth 7, (b) Growth 20, (b) Growth 21.

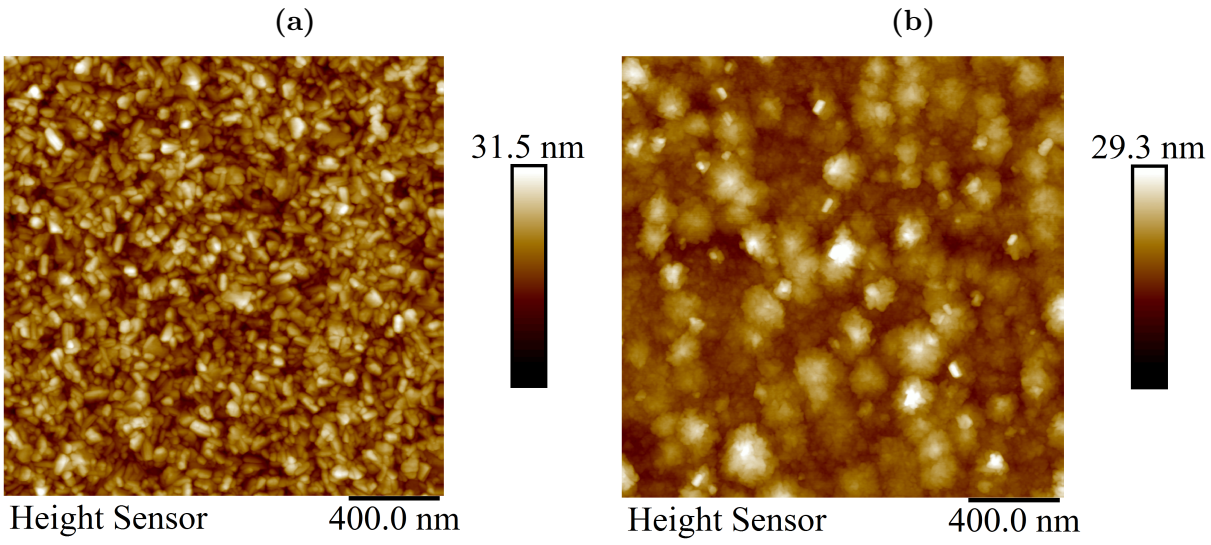


Figure 17: Atomic Force Microscope images of films from: (a) Growth 7, (b) Growth 21

# 7 Conclusion and Outlook

In this work, the growth behaviour of gallium oxide thin films deposited on 4H-SiC substrates by PLD was investigated as a function of process pressure, growth temperature, fluence, and laser pulse frequency. Based on this study, the growth conditions were progressively optimised to improve the film crystal quality, growth rate, and surface morphology.

The optimised heteroepitaxial film, Growth 21, was 108.07±0.33 nm thick, exhibited a growth rate of 10.81 pm/pulse, had a relatively smooth surface morphology ($R_q = 2.5$ nm), and a narrow $(\bar{2}01)$ rocking curve FWHM value of 1.627°± 0.034°. The introduction of an argon-grown buffer layer was found to be crucial for achieving high crystalline quality heteroepitaxial growth of gallium oxide on SiC. The buffer layer suppresses oxidation of the SiC surface during the initial growth stage, thereby preventing the formation of an amorphous interfacial layer that would otherwise degrade the epitaxial quality of the subsequently grown film. Furthermore, increasing the thickness of the argon-grown buffer layer were found to further improve the crystalline quality of the overall film.

The limited time duration of this thesis did not allow for a more extensive investigation of the roles of laser fluence and laser frequency on the growth behaviour. Additional data points for these two parameter series would have been useful in establishing more definite trends, enabling further optimisation of the growth conditions. In particular, optimisation of both the growth rate and crystallinity of the buffer layer remains necessary and was beyond the scope of the present work. Lower buffer-layer growth temperatures may enhance the buffer-layer growth rate while still maintaining its structural function.

In this work, substrate pre-treatment consisted of sequential cleaning in acetone, isopropanol (IPA), and deionised (DI) water to remove organic surface contamination. A more thorough substrate pre-treatment procedure would additionally include RCA1 and RCA2 cleaning processes for more effective removal of organic contaminants [46], followed by a concentrated hydrofluoric acid (HF) dip to remove the oxide prior to growth. This enhanced substrate pre-treatment is expected to yield cleaner, chemically better-defined SiC substrates, thereby promoting improved epitaxial growth and higher crystalline quality gallium oxide films.

## References


[1] M. Bosi et al. "Ga2O3 polymorphs: tailoring the epitaxial growth conditions". en. In: *Journal of Materials Chemistry C* 8.32 (Aug. 2020), pp. 10975–10992. ISSN: 2050-7534. DOI: 10.1039/D0TC02743J. URL: https://pubs.rsc.org/en/content/articlelanding/2020/tc/d0tc02743j (visited on 02/17/2026).

[2] Yuhao Zhang et al. "Wide-bandgap semiconductors and power electronics as pathways to carbon neutrality". en. In: *Nature Reviews Electrical Engineering* 2.3 (Mar. 2025), pp. 155–172. ISSN: 2948-1201. DOI: 10.1038/s44287-024-00135-5. URL: https://www.nature.com/articles/s44287-024-00135-5 (visited on 05/05/2026).

[3] Ruizhe Zhang and Yuhao Zhang. "Power device breakdown mechanism and characterization: review and perspective". en. In: *Japanese Journal of Applied Physics* (Apr. 2023). ISSN: 0021-4922. URL: http://hdl.handle.net/10919/116325 (visited on 03/02/2026).

[4] Huiqi Zhao et al. "An enhanced intrusion detection method for AIM of smart grid". en. In: *Journal of Ambient Intelligence and Humanized Computing* 14.5 (May 2023), pp. 4827–4839. ISSN: 1868-5145. DOI: 10.1007/s12652-023-04538-4. URL: https://link.springer.com/article/10.1007/s12652-023-04538-4 (visited on 05/28/2026).

[5] B R Tak et al. "Recent advances in the growth of gallium oxide thin films employing various growth techniques—a review". en. In: *Journal of Physics D: Applied Physics* 54.45 (Aug. 2021), p. 453002. ISSN: 0022-3727. DOI: 10.1088/1361-6463/ac1af2. URL: https://doi.org/10.1088/1361-6463/ac1af2 (visited on 02/17/2026).

[6] Dr Rüdiger Paschotta. "Solar-blind Photodetectors". en. In: *RP Photonics Encyclopedia* (June 2019). DOI: 10.61835/yez. URL: https://www.rp-photonics.com/solar_blind_photodetectors.html (visited on 02/17/2026).

[7] Andrew Green et al. "Roadmap: -Gallium oxide power electronics". In: *APL Materials* 10 (Feb. 2022), p. 029201. DOI: 10.1063/5.0060327.

[8] Jean-Pierre Brog et al. "Polymorphism, what it is and how to identify it: a systematic review". en. In: *RSC Advances* 3.38 (Sept. 2013), pp. 16905–16931. ISSN: 2046-2069. DOI: 10.1039/C3RA41559G. URL: https://pubs.rsc.org/en/content/articlelanding/2013/ra/c3ra41559g (visited on 02/26/2026).

[9] Ildikó Cora et al. "The real structure of -Ga2O3 and its relation to -phase". en. In: *CrystEngComm* 19.11 (Mar. 2017), pp. 1509–1516. ISSN: 1466-8033. DOI: 10.1039/C7CE00123A. URL: https://pubs.rsc.org/en/content/articlelanding/2017/ce/c7ce00123a (visited on 03/02/2026).

[10] Dinusha Herath Mudiyanselage et al. "-Ga2O3-Based Heterostructures and Heterojunctions for Power Electronics: A Review of the Recent Advances". en. In: *Electronics* 13.7 (Mar. 2024). ISSN: 2079-9292. DOI: 10.3390/electronics13071234. URL: https://www.mdpi.com/2079-9292/13/7/1234 (visited on 03/02/2026).

[11] Haechan Kim et al. "Structural and Electrical Properties of Si-Doped -Ga2O3 Thin Films Deposited by RF Sputtering: Effects of Oxygen Flow Ratio and Post-Annealing Temperature". en. In: *Coatings* 15.10 (Oct. 2025), p. 1181. ISSN: 2079-6412. DOI: 10.3390/coatings15101181. URL: https://www.mdpi.com/2079-6412/15/10/1181 (visited on 05/05/2026).

[12] Mahitosh Biswas and Hiroyuki Nishinaka. "Thermodynamically metastable -, - (or -), and -Ga2O3: From material growth to device applications". In: *APL Materials* 10.6 (June 2022), p. 060701. ISSN: 2166-532X. DOI: 10.1063/5.0085360. URL: https://doi.org/10.1063/5.0085360 (visited on 02/17/2026).

[13] Sudip K. Mazumder et al. "Overview of Wide/Ultrawide Bandgap Power Semiconductor Devices for Distributed Energy Resources". In: *IEEE Journal of Emerging and Selected Topics in Power Electronics* 11.4 (Aug. 2023), pp. 3957–3982. ISSN: 2168-6785. DOI: 10.1109/JESTPE.2023.3277828. URL: https://ieeexplore.ieee.org/document/10129950 (visited on 05/05/2026).

[14] J. Y. Tsao et al. "Ultrawide-Bandgap Semiconductors: Research Opportunities and Challenges". en. In: *Advanced Electronic Materials* 4.1 (2018), p. 1600501. ISSN: 2199-160X. DOI: 10.1002/aelm.201600501. URL: https://onlinelibrary.wiley.com/doi/abs/10.1002/aelm.201600501 (visited on 05/05/2026).

[15] Jeffrey Morroni and Pradeep Shenoy. *Understanding the Trade-Offs Between On-State Resistance and Switching Losses in Power MOSFETs*. URL: https://www.ti.com/lit/slyy193 (visited on 03/02/2026).

[16] S. J. Pearton et al. "Perspective: Ga2O3 for ultra-high power rectifiers and MOSFETS". In: *Journal of Applied Physics* 124.22 (Dec. 2018), p. 220901. ISSN: 0021-8979. DOI: 10.1063/1.5062841. URL: https://doi.org/10.1063/1.5062841 (visited on 03/02/2026).

[17] Seokje Lee et al. "GaN remote epitaxy on a pristine graphene buffer layer via controlled graphitization of SiC". In: *Applied Physics Letters* 125.25 (Dec. 2024), p. 252102. ISSN: 0003-6951. DOI: 10.1063/5.0235653. URL: https://doi.org/10.1063/5.0235653 (visited on 05/05/2026).

[18] Nick A. Shepelin et al. "A practical guide to pulsed laser deposition". en. In: *Chemical Society Reviews* 52.7 (Apr. 2023), pp. 2294–2321. ISSN: 1460-4744. DOI: 10.1039/D2CS00938B. URL: https://pubs.rsc.org/en/content/articlelanding/2023/cs/d2cs00938b (visited on 02/17/2026).

[19] H. von Wenckstern et al. "Fundamentals of pulsed laser deposition, advanced developments and implementation of combinatorial material synthesis, and its application to the growth of Ga2O3 and related alloys". en-US. In: *Comprehensive Semiconductor Science and Technology (Second Edition)* (Jan. 2025), pp. 225–266. DOI: 10.1016/B978-0-323-96027-4.00042-5. URL: https://www.sciencedirect.com/science/chapter/referencework/pii/B9780323960274000425 (visited on 02/17/2026).

[20] Roshna S. H. *Pulsed Laser Deposition Technique*. en-US. Apr. 2024. URL: https://intuitivetutorial.com/2024/04/12/pulsed-laser-deposition-technique-for-thin-film-growth/ (visited on 03/02/2026).

[21] Jixiang Cai et al. "Application of Pulsed Laser Deposition (PLD) Technology in the Preparation of Two-Dimensional (2D) Film Materials". en. In: *Materials* 18.13 (June 2025). ISSN: 1996-1944. DOI: 10.3390/ma18132999. URL: https://www.mdpi.com/1996-1944/18/13/2999 (visited on 03/02/2026).

[22] S. J Guilfoyle et al. "Modelling of pulsed laser deposition of large area films". In: *Journal of Magnetism and Magnetic Materials* 198-199 (June 1999), pp. 113–115. ISSN: 0304-8853. DOI: 10.1016/S0304-8853(98)01030-0. URL: https://www.sciencedirect.com/science/article/pii/S0304885398010300 (visited on 05/14/2026).

[23] *Epitaxy — Crystal Growth & Characteristics — Britannica*. URL: https://www.britannica.com/science/epitaxy (visited on 03/04/2026).

[24] M. Suemitsu and S. N. Filimonov. "3 - Understanding crystal growth mechanisms in silicon–germanium (SiGe) nanostructures". In: *Silicon–Germanium (SiGe) Nanostructures*. Ed. by Yasuhiro Shiraki and Noritaka Usami. Woodhead Publishing Series in Electronic and Optical Materials. Woodhead Publishing, 2011, pp. 45–71. ISBN: 978-1-84569-689-4. DOI: https://doi.org/10.1533/9780857091420.2.45. URL: https://www.sciencedirect.com/science/article/pii/B9781845696894500031.

[25] Prasanta K. Misra. "Chapter 1 - Basic Properties of Crystals". In: *Physics of Condensed Matter*. Ed. by Prasanta K. Misra. Boston: Academic Press, 2012, pp. 1–35. ISBN: 978-0-12-384954-0. DOI: https://doi.org/10.1016/B978-0-12-384954-0.00001-3. URL: https://www.sciencedirect.com/science/article/pii/B9780123849540000013.

[26] Bei Xu et al. "Study of the Bonding Characteristics at -Ga2O3(201)/4H-SiC(0001) Interfaces from First Principles and Experiment". en. In: *Crystals* 13.2 (Feb. 2023), p. 160. ISSN: 2073-4352. DOI: 10.3390/cryst13020160. URL: https://www.mdpi.com/2073-4352/13/2/160 (visited on 05/05/2026).

[27] Udo W. Pohl. "Thermodynamics of Epitaxial Layer-Growth". en. In: *Epitaxy of Semiconductors: Introduction to Physical Principles*. Ed. by Udo W. Pohl. Berlin, Heidelberg: Springer, 2013, pp. 131–170. ISBN: 978-3-642-32970-8. DOI: 10.1007/978-3-642-32970-8_4. URL: https://doi.org/10.1007/978-3-642-32970-8_4 (visited on 02/17/2026).

[28] Débora Gonçalves and Eugene A. Irene. "Fundamentals and applications of spectroscopic ellipsometry". en. In: *Química Nova* 25 (2002), pp. 794–800. ISSN: 0100-4042, 1678-7064. DOI: https://doi.org/10.1590/S0100-40422002000500015. URL: https://www.scielo.br/j/qn/a/mMdqrt7dbFT7Bbc3cRqfJzj/?lang=en (visited on 04/04/2026).

[29] Abed et al. *Role of substrate temperature on the performance of BaTiO3/Si photodetector prepared by pulsed laser deposition — Scientific Reports*. URL: https://www.nature.com/articles/s41598-024-55053-1 (visited on 03/10/2026).

[30] Weijia Yang et al. "Effect of target–substrate distance on the quality of AlN films grown on Si(110) substrates by pulsed laser deposition". In: *Materials Letters* 160 (Dec. 2015), pp. 20–23. ISSN: 0167-577X. DOI: 10.1016/j.matlet.2015.07.069. URL: https://www.sciencedirect.com/science/article/pii/S0167577X15302664 (visited on 03/10/2026).

[31] George F. Harrington and José Santiso. "Back-to-Basics tutorial: X-ray diffraction of thin films". en. In: *Journal of Electroceramics* 47.4 (Dec. 2021), pp. 141–163. ISSN: 1573-8663. DOI: 10.1007/s10832-021-00263-6. URL: https://doi.org/10.1007/s10832-021-00263-6 (visited on 02/17/2026).

[32] Asif Ali, Yi Wai Chiang, and Rafael M. Santos. "X-ray Diffraction Techniques for Mineral Characterization: A Review for Engineers of the Fundamentals, Applications, and Research Directions". en. In: *Minerals* 12.2 (Feb. 2022). ISSN: 2075-163X. DOI: 10.3390/min12020205. URL: https://www.mdpi.com/2075-163X/12/2/205 (visited on 03/11/2026).

[33] Sim et al. Kok Swee. *Signal-to-Noise Ratio in Scanning Electron Microscopy: A Comprehensive Review — IEEE Journals & Magazine — IEEE Xplore*. URL: https://ieeexplore.ieee.org/document/11142276 (visited on 03/11/2026).

[34] Sven Henning and Rameshwar Adhikari. "Scanning Electron Microscopy, ESEM, and X-ray Microanalysis". en-US. In: *Microscopy Methods in Nanomaterials Characterization*. Elsevier, Jan. 2017, pp. 1–30. DOI: 10.1016/B978-0-323-46141-2.00001-8. URL: https://www.sciencedirect.com/science/chapter/edited-volume/pii/B9780323461412000018 (visited on 05/08/2026).

[35] Raghvendra Kumar Mishra, Ajesh K. Zachariah, and Sabu Thomas. "Chapter 12 - Energy-Dispersive X-ray Spectroscopy Techniques for Nanomaterial". In: *Microscopy Methods in Nanomaterials Characterization*. Ed. by Sabu Thomas et al. Elsevier, Jan. 2017, pp. 383–405. ISBN: 978-0-323-46141-2. DOI: 10.1016/B978-0-323-46141-2.00012-2. URL: https://www.sciencedirect.com/science/article/pii/B9780323461412000122.

[36] Wojciech Ogieglo et al. "Spectroscopic Ellipsometry analysis of a thin film composite membrane consisting of polysulfone on a porous -alumina support". English. In: *ACS Applied Materials and Interfaces* 4.2 (2012), pp. 935–943. ISSN: 1944-8244. DOI: 10.1021/am2015958. URL: https://research.utwente.nl/en/publications/spectroscopic-ellipsometry-analysis-of-a-thin-film-composite-memb/ (visited on 03/11/2026).

[37] Grazia Giuseppina Politano and Carlo Versace. "Spectroscopic Ellipsometry: Advancements, Applications and Future Prospects in Optical Characterization". en. In: *Spectroscopy Journal* 1.3 (Dec. 2023), pp. 163–181. ISSN: 2813-446X. DOI: 10.3390/spectroscj1030014. URL: https://www.mdpi.com/2813-446X/1/3/14 (visited on 04/04/2026).

[38] *CompleteEASE Software Manual — PDF — Applied And Interdisciplinary Physics — Optics*. en. URL: https://www.scribd.com/document/872548366/CompleteEASE-6-Manual (visited on 05/11/2026).

[39] Krzysztof Dorywalski, Igor Maciejewski, and Tomasz Krzyżyński. "Spectroscopic ellipsometry technique as a materials characterization tool for mechatronic systems—The case

of composition and doping concentration monitoring in SBN crystals". In: *Mechatronics*. THEORETICAL AND APPLIED ASPECTS OF MODERN MECHATRONICS 37 (Aug. 2016), pp. 33–41. ISSN: 0957-4158. DOI: 10.1016/j.mechatronics.2015.11.005. URL: https://www.sciencedirect.com/science/article/pii/S0957415815001981 (visited on 05/28/2026).

[40] Mohamed A. Hafez, Mohamed K. Zayed, and Hani E. Elsayed-Ali. "Review: Geometric interpretation of reflection and transmission RHEED patterns". In: *Micron* 159 (Aug. 2022), p. 103286. ISSN: 0968-4328. DOI: 10.1016/j.micron.2022.103286. URL: https://www.sciencedirect.com/science/article/pii/S0968432822000828 (visited on 04/09/2026).

[41] Shuji Hasegawa. *Reflection High-Energy Electron Diffraction*. Oct. 2012. ISBN: 978-0-471-26696-9. DOI: 10.1002/0471266965.com139.

[42] Udo W. Pohl. "Structural Properties of Heterostructures". In: *Epitaxy of Semiconductors: Introduction to Physical Principles*. Berlin, Heidelberg: Springer Berlin Heidelberg, 2013, pp. 11–77. ISBN: 978-3-642-32970-8. DOI: 10.1007/978-3-642-32970-8_2. URL: https://doi.org/10.1007/978-3-642-32970-8_2.

[43] Ricardo García and Rubén Pérez. "Dynamic atomic force microscopy methods". In: *Surface Science Reports* 47.6 (Sept. 2002), pp. 197–301. ISSN: 0167-5729. DOI: 10.1016/S0167-5729(02)00077-8. URL: https://www.sciencedirect.com/science/article/pii/S0167572902000778 (visited on 05/08/2026).

[44] Nader Jalili and Karthik Laxminarayana. "A review of atomic force microscopy imaging systems: application to molecular metrology and biological sciences". In: *Mechatronics* 14.8 (Oct. 2004), pp. 907–945. ISSN: 0957-4158. DOI: 10.1016/j.mechatronics.2004.04.005. URL: https://www.sciencedirect.com/science/article/pii/S0957415804000455 (visited on 05/08/2026).

[45] Hsueh-I Chen et al. "Epitaxial growth of TiN on (0001) semi-insulating 4H-SiC substrate by reactive sputtering". In: *Surface and Coatings Technology* 437 (May 2022), p. 128357. ISSN: 0257-8972. DOI: 10.1016/j.surfcoat.2022.128357. URL: https://www.sciencedirect.com/science/article/pii/S025789722200278X (visited on 05/09/2026).

[46] Steven Verhaverbeke, Jennifer W. Parker, and Chris F. McConnell. "The Role of HO2 in SC-1 Cleaning Solutions". en. In: *MRS Online Proceedings Library (OPL)* 477 (Jan. 1997), p. 47. ISSN: 1946-4274. DOI: 10.1557/PROC-477-47. URL: https://www.cambridge.org/core/journals/mrs-online-proceedings-library-archive/article/abs/role-of-ho2-in-sc1-cleaning-solutions/C9ED3A62A16531625529E74D9FC5FE9C (visited on 05/14/2026).

# A Appendix

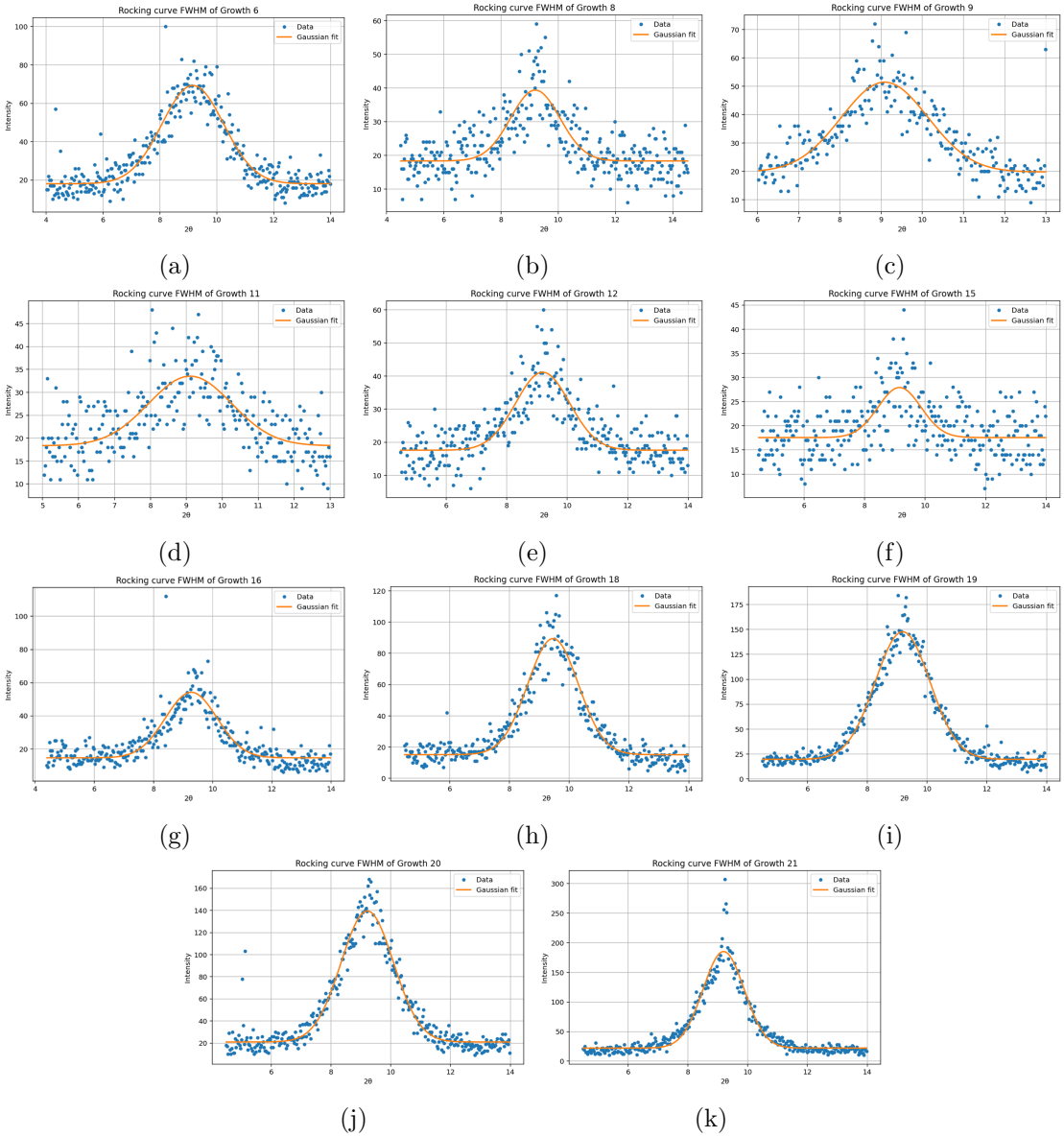


Figure A.1: FWHM of Gaussian curve fit on Rocking Curve data of $\bar{2}01$ peak for growth runs (a) 6, (b) 8, (c) 9, (d) 11, (e) 12, (f) 15, (g) 16, (h) 18, (i) 19, (j) 20, (k) 21.

| Growth Run | Thickness of Thin Film (nm) | MSE | Growth rate (pm/p) |
|---|---|---|---|
| 6 | $97.60 \pm 0.13$ | 6.145 | 19.80 |
| 7 | $128.44 \pm 0.05$ | 8.006 | 25.69 |
| 8 | $53.60 \pm 0.08$ | 4.730 | 10.72 |
| 9 | $73.07 \pm 0.12$ | 5.406 | 14.61 |
| 11 | $53.47 \pm 0.11$ | 4.576 | 10.69 |
| 12 | $44.15 \pm 0.01$ | 4.650 | 8.83 |
| 13 | $33.90 \pm 0.54$ | 3.921 | 6.78 |
| 14 | $15.86 \pm 0.02$ | 4.313 | 3.17 |
| 15 | $27.51 \pm 0.03$ | 4.899 | 5.50 |
| 16 | $62.11 \pm 0.04$ | 4.805 | 12.42 |
| 17 | $48.30 \pm 0.10$ | 3.451 | 9.66 |
| 18 | $94.07 \pm 0.14$ | 5.190 | 18.81 |
| 19 | $121.23 \pm 0.27$ | 8.188 | 24.25 |
| 20 | $139.87 \pm 0.38$ | 50.981 | 27.97 |
| 21 | $108.07 \pm 0.33$ | 8.500 | 10.81 |

Table A.1: Thin film thickness and mean squared error (MSE) values for different growth runs.

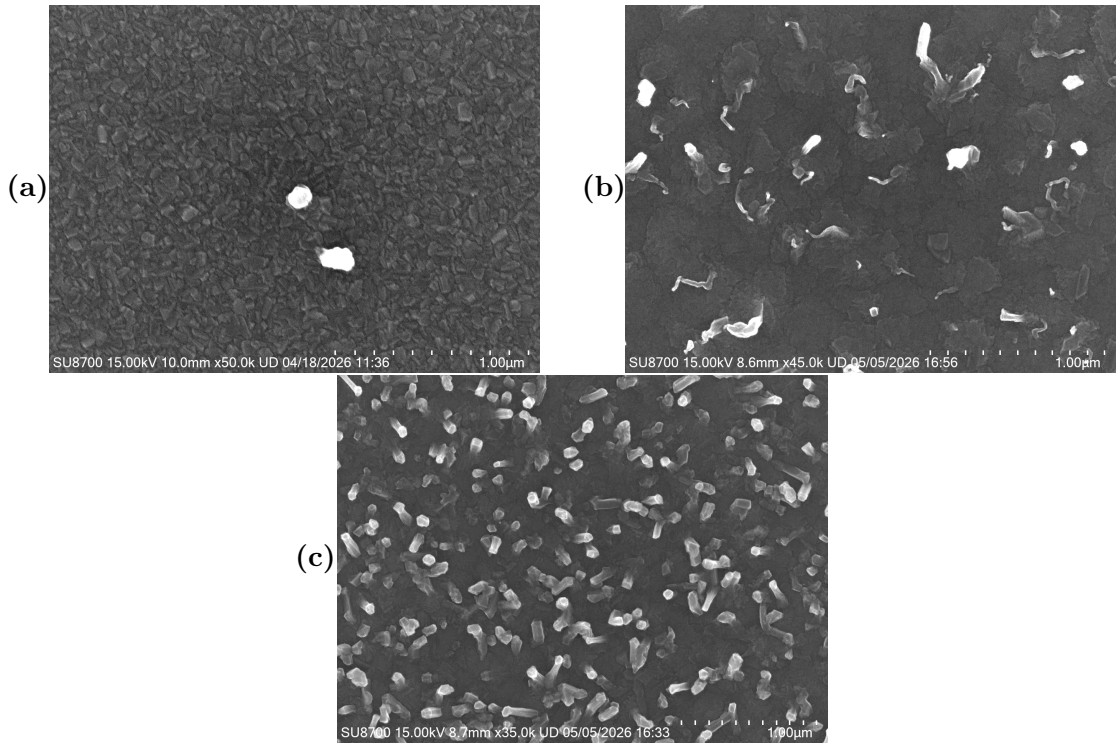


Figure A.2: Scanning Electron Microscope images (zoomed-in) of: (a) Growth 7, (b) Growth 21, (c) Growth 20.

| Peak Angle | Peak Center ($2\theta$) | Error | Amplitude (Counts) |
|---|---|---|---|
| 35.583° | 35.609° | 0.0091° | 53694.9 |
| 75.333° | 75.365° | 0.0051° | 18426.2 |

Table A.2: Peak fitting for Growth 7 $2\theta/\omega$ scan .

| Peak Center ($2\theta$) | $\beta - Ga_2O_3$ Plane | Error | Amplitude (Counts) |
|---|---|---|---|
| 18.911° | (-201) | 0.0013° | 45.3 |
| 35.583° | - | 0.0133° | 108273.1 |
| 38.332° | (-402) | 0.0026° | 12.0 |
| 59.058° | (-603) | 0.0044° | 10.9 |
| 75.333° | - | 0.0054° | 26136.4 |

Table A.3: Peak fitting for Growth 6 $2\theta/\omega$ scan .

| Growth Run | FWHM of (-201) Peak (°) | Error | Peak Centre (°) |
|---|---|---|---|
| 6 | 2.56083 | 0.07552 | 9.15866 |
| 8 | 2.02834 | 0.12463 | 9.19675 |
| 9 | 2.48472 | 0.13395 | 9.08669 |
| 11 | 2.72481 | 0.23553 | 9.10529 |
| 12 | 2.09752 | 0.10800 | 9.18774 |
| 15 | 1.67437 | 0.18944 | 9.15408 |
| 16 | 2.05817 | 0.08368 | 9.27329 |
| 18 | 1.99757 | 0.04267 | 9.45996 |
| 19 | 2.16281 | 0.02976 | 9.18259 |
| 20 | 2.06705 | 0.03912 | 9.21671 |
| 21 | 1.62739 | 0.03354 | 9.19613 |

Table A.4: FWHM and peak centre values for the $(-201)$ peak from different growth runs.

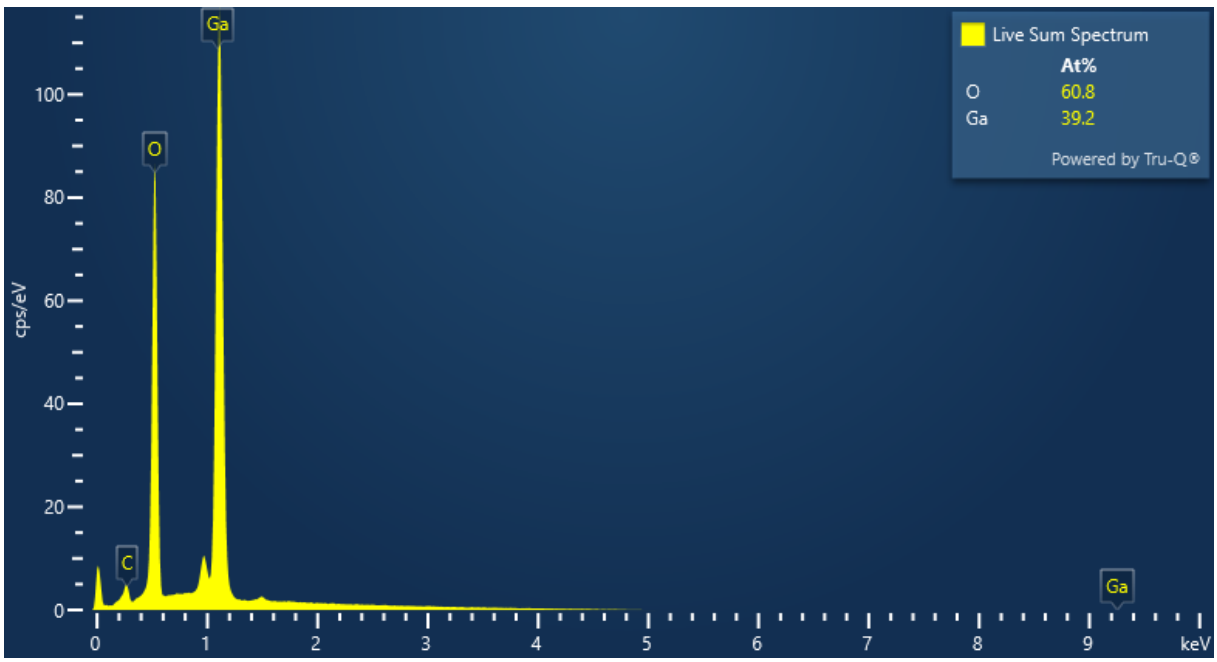


Figure A.3: EDS scan of Growth 6.

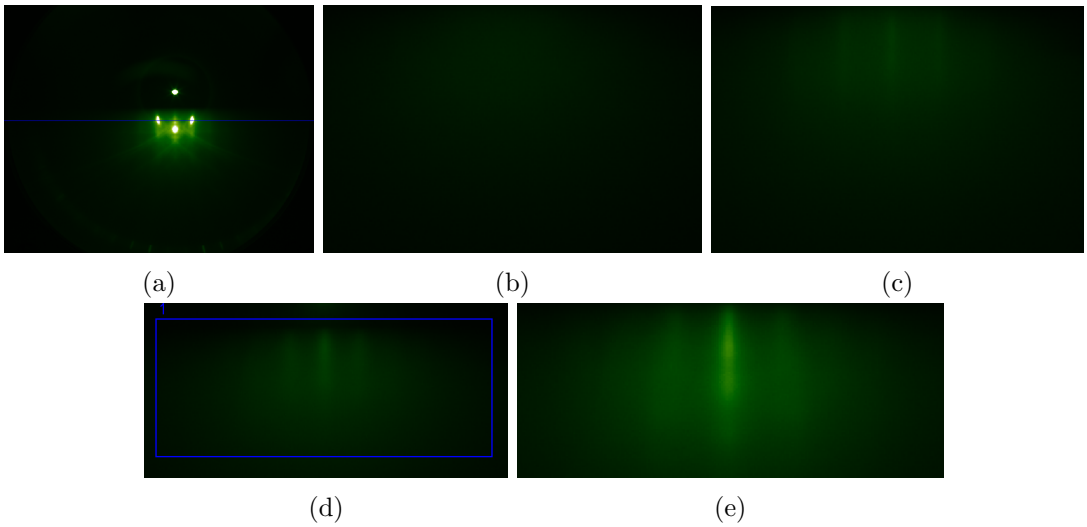


Figure A.4: RHEED images of Growth run 6 (without buffer): (a) before growth, (b) at 500 laser pulses, (c) at 1200 laser pulses, (d) at 1800 laser pulses, (e) 5000 pulses, after growth had completed.

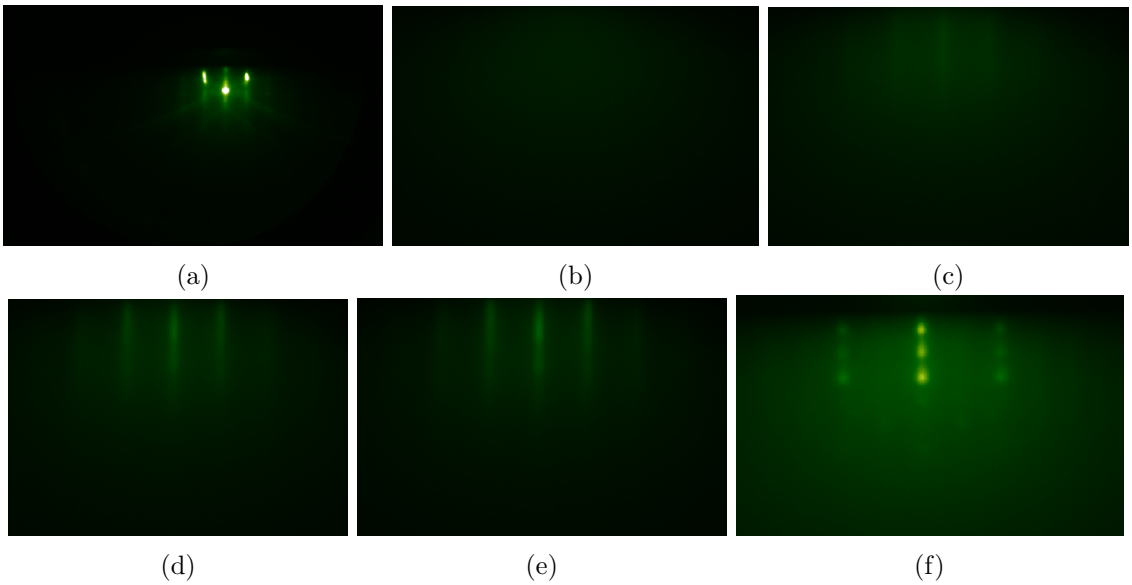


Figure A.5: RHEED images of Growth run 16 (with buffer): (a) before growth, (b) at 330 laser pulses, (c) at 1000 laser pulses, (d) at 1400 laser pulses, (e) at 1700 laser pulses, (f) after the growth has completed. Since clear columns were seen at 1700 pulses, this was the chosen number of pulses for the buffer layer growth.

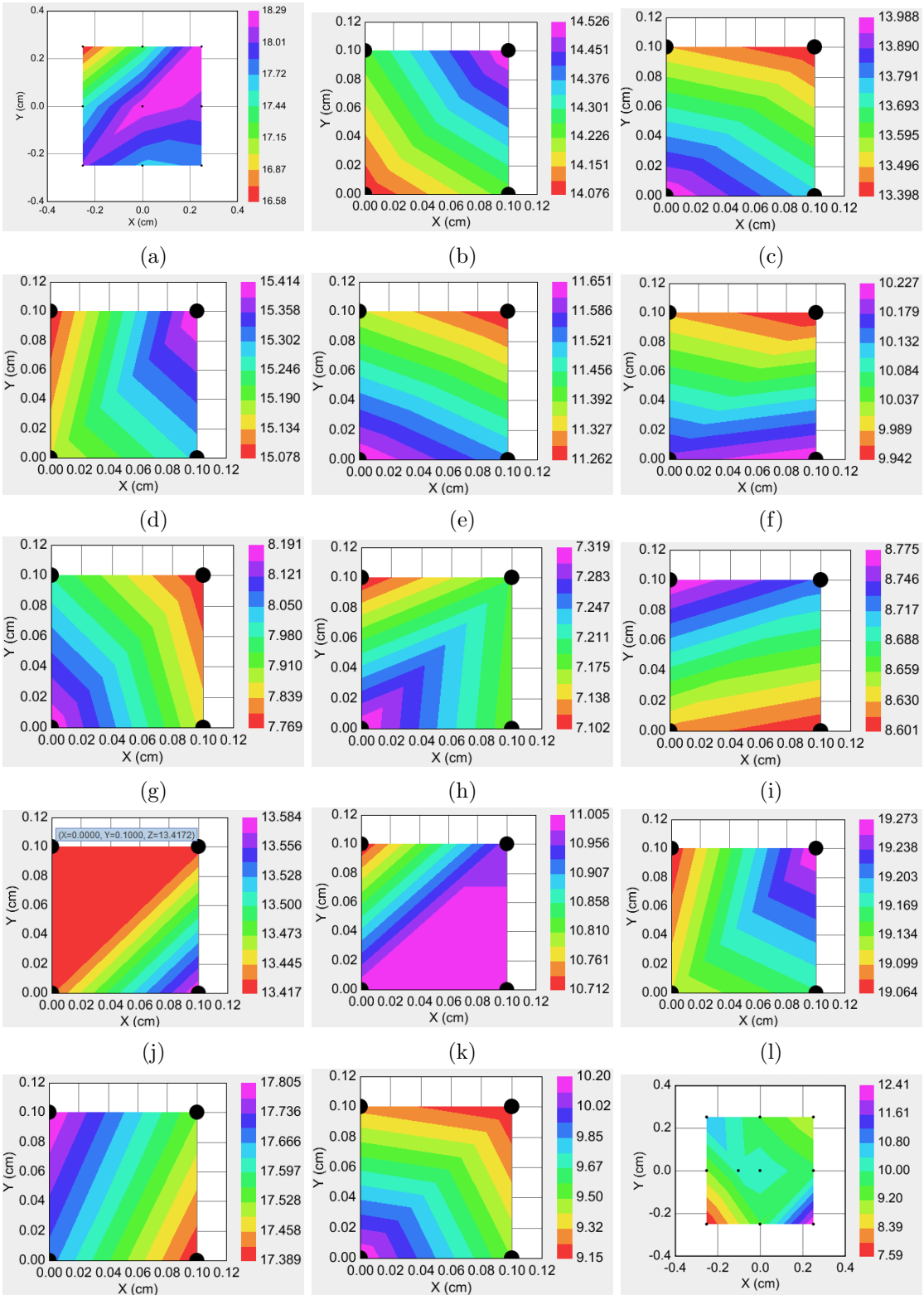


Figure A.6: Thickness distribution maps of growth: (a) 6, (b) 7, (c) 8, (d) 9, (e) 11, (f) 12, (g) 13, (h) 14, (i) 15, (j) 16, (k) 17, (l) 18, (m) 19, (n) 20, (o) 21 from the spectroscopic ellipsometer.